ACCURATE POLARIZATION CALIBRATION AT 800 MHZ WITH THE GREEN BANK TELESCOPE

Yu-Wei Liao[1], Tzu-Ching Chang[1], Cheng-Yu Kuo[1,2], Kiyoshi Wesley Masui[3,4], Niels Oppermann[5], Ue-Li Pen[5], and Jeffrey B. Peterson[6]

Draft version October 1, 2018

ABSTRACT

Polarization leakage of foreground synchrotron emission is a critical issue in HI intensity mapping experiments. While the sought-after HI emission is unpolarized, polarized foregrounds such as Galactic and extragalactic synchrotron radiation, if coupled with instrumental impurity, can mimic or overwhelm the HI signals. In this paper we present the methodology for polarization calibration at 700-900 MHz, applied on data obtained from the Green Bank Telescope (GBT). We use astrophysical sources, both polarized and unpolarized sources including quasars and pulsars, as calibrators to characterize the polarization leakage and control systematic effects in our GBT HI intensity mapping project. The resulting fractional errors on polarization measurements on boresight are well controlled to within 0.6%-0.8% of their total intensity. The polarized beam patterns are measured by performing spider scans across both polarized quasars and pulsars. A dominant Stokes I to V leakage feature and secondary features of Stokes I to Q and I to U leakages in the 700-900 MHz frequency range are identified. These characterizations are important for separating foreground polarization leakage from the HI 21 cm signal.

Subject headings: Astronomical Instrumentation

1. INTRODUCTION

Neutral hydrogen (HI) is one of the most promising probes of the high-redshift universe. It can be used to uniquely trace the matter distribution at early times well into the dark ages and the cosmic dawn era, reveal the cosmic reionization process and shed light on the complex astrophysics in early galaxy formation, and probe the large-scale structure at late times, allowing measurements of the geometry and structure growth of the universe. To obtain statistical measurement of the three-dimensional structure of HI in emission, the intensity mapping technique has been advocated (e.g., Chang et al. (2008), Loeb & Wyithe (2008), Chang et al. (2010)). Making use of the redshifted 21 cm HI intensity mapping dataset obtained at the Green Bank Telescope (GBT), Masui et al. (2013) and Switzer et al. (2013) have measured the HI crosspower spectrum with the WiggleZ optical galaxies and reported limits on the HI auto-power spectrum, respectively, in the frequency range of 700-900 MHz or a redshifted HI range of $0.6 < z < 1$. Combining the crosspower and auto-power spectrum, the neutral hydrogen fluctuation amplitude, $\Omega_{HI}b_{HI}$ has been constrained as $\Omega_{HI}b_{HI} = [0.62^{+0.23}_{-0.15}] \times 10^{-3}$.

The main challenges of HI intensity mapping at these redshifts include synchrotron foreground radiation and man-made radio frequency interference (RFI). Localized synchrotron emission from extragalactic sources and diffuse synchrotron emission from the interstellar medium (ISM) in the Milky Way are the dominant astronomical foreground signals in the frequency range of interest. In the GBT HI observing fields reported by Switzer et al. (2013), which are at high Galactic latitudes, the synchrotron emission is still three orders of magnitude brighter than the 21 cm signals. However, synchrotron radiation is expected to be spectrally smooth (Oh and Mack (2003); Seo et al. (2010)). If all the instrumental effects, including calibration, spectral response, and primary beam pattern, are well understood and controlled, the synchrotron foregrounds will then have fewer degrees of freedom than the HI signals along the line of sight, or along the frequency direction, and can be separated. In the GBT data, RFI is found to be removable or controllable by flagging of frequency channels.

A crucial instrumental effect that needs to be controlled is polarization leakage. Although HI emission is considered unpolarized, the leakage of polarized synchrotron foreground emission into total intensity via imperfect instrumental response could introduce excess power and extra degrees of freedom into the observed intensity signal. Simulations suggest polarized intensity of Galactic Foregrounds can contain frequency structure via Faraday rotation induced by the ISM; leakages of such spectrally fluctuating polarization intensity into total intensity could thus mimic the HI signals along the frequency or redshift direction (Jelić et al. (2010), Moore et al. (2013)). Furthermore, polarization leakage itself may not be a smooth function of frequency. Therefore, one may not be able to simply separate polarization leakage from HI signals by isolating spectrally smooth patterns.

[1] Institute of Astronomy and Astrophysics, Academia Sinica, 11F of Astro-Math Building, AS/NTU, 1 Roosevelt Rd Sec. 4, Taipei 10617, Taiwan; ywliao@asiaa.sinica.edu.tw
[2] Department of Physics, National Sun Yat-Sen University, 70 Lienhai Road, Kaohsiung 80424, Taiwan
[3] Department of Physics and Astronomy, University of British Columbia, Vancouver, British Columbia, V6T 1Z1, Canada
[4] Canadian Institute for Advanced Research, CIFAR Program in Cosmology and Gravity, Toronto, Ontario, M5G 1Z8, Canada
[5] Canadian Institute for Theoretical Astrophysics, University of Toronto, 60 St. George Street, Toronto ON, M5S 3H8, Canada
[6] McWilliams Center for Cosmology, Carnegie Mellon University, Department of Physics, 5000 Forbes Ave., Pittsburgh PA 15213, USA

The polarized Galactic foreground is one to two orders of magnitude fainter than total intensity in regions with low Galactic synchrotron emission at the frequency of interest. The amplitude in total intensity due to polarization leakage would be comparable to that of the HI signals if the leakage fraction is at the percentage level, which is common in single dish radio telescopes (Martí-Vidal et al. 2012). Therefore, polarization calibration needs to be performed very carefully to eliminate the contamination from polarized foreground signals.

Recent investigation of LOFAR polarization leakage by Asad et al. (2015) provides a good estimate of polarization calibration errors (less than 0.005%) of inflicted on the HI signal of interest at 150 MHz. As an interferometer, the redundancy of LOFAR baselines dramatically reduces the integrated polarization calibration errors; this is however not the case for single dish telescopes. Besides, Moore et al. (2015) suggest that the foreground polarization fraction at $\sim$ 150 MHz is one order of magnitude lower than that at 1.4 GHz. Polarization calibration with single dishes is potentially a challenge at 800 MHz.

Performing polarization calibration with a signal dish radio telescope with dual receptors, such as the GBT, usually entails determining the Jones matrix, which describes the instrumental response of the two polarization receptors to sky signals at each frequency channel. Polarized astrophysical sources are often used to solve for the Jones matrices (e.g.: Heiles (2001) and van Straten (2004)). PSRCHIVE (Hotan et al. (2004)), a software that is widely used for single dish radio polarization calibration in the pulsar community, uses pulsar observations at multiple parallactic angles to solve for the Jones matrix at each frequency channel. In this work, we use the Jones matrix model described by van Straten (2004), which is adopted in PSRCHIVE, to parametrize Jones matrices. We obtain both pulsar and quasar observations from the GBT. We first solve for the first-order approximation to the Jones matrix model parameters using pulsar data and the PSRCHIVE software, then fine tune the parameters using quasar observations. We begin with a brief introduction to GBT 800 MHz receiver and the back-end systems we use in this work in Section 2. The polarization calibration on boresight is discussed in detail in Section 3.

Besides polarization leakage on boresight, another key element is to characterize the polarized primary beam pattern of a telescope. Pulsar observations have the adventage that it is easy to separate on-axis pulsar signal and stationary off-axis leakage by subtracting off-pulse from on-pulse data. On the other hand, since both on-axis signal and off-axis leakage are stationary in our intensity mapping observations, off-axis leakage is therefore an issue that needs to be addressed. In Section 4, we use spider scans of quasars and pulsars to investigate the polarization beam pattern of the GBT. These patterns are important for the interpretation of the HI intensity mapping power spectrum. The procedure we are using to calibrate real data is summarized in Section 5. We will discuss the results and limits of our investigation in Section 6.

2. GBT 800 MHZ RECEIVER AND GUPPI BACKEND

Here we briefly describe the GBT 800 MHz receiver and backend system. The GBT has an off-axis optical design; the 800 MHz receiver is a prime-focus instrument that operates at 680-920 MHz. The feed is a corrugated feed horn with an Orthomode transducer (OMT) polarization splitter. There are known resonances associated with the OMT at 796.6 MHz and 817.4 MHz, which we omit from the analysis. A noise diode signal is injected after the OMT at 2 K level and switches at 15.26 Hz. We use the Green Bank Ultimate Pulsar Processing Instrument (GUPPI) pulsar back-end systems (DuPlain et al. 2008), with a bandwidth of 200 MHz (700-900 MHz) over 4096 frequency channels, and integrate over 1 ms intervals. GUPPI has the pulsar-folding capability which we use in our analysis. See Masui et al. (2013) for more details.

3. POLARIZATION CALIBRATION

In this section we present the method for polarization calibration at the beam center, or boresight, without considering the angular response of the primary beam. We adopt the model described by van Straten (2004) to parametrize the Jones matrix and use quasar and pulsar observations to find solutions for the Jones matrix parameters. We then apply the parameters on quasar data to further correct for polarization leakage.

3.1. Mueller/Jones matrix model

In the following sections we follow Britton (2000) and van Straten (2004) to model the Jones matrix. The mapping between the real sky electric field signal $\boldsymbol{S}_{\mathrm{E}} = (E_x, E_y)$ and the observed signal $\boldsymbol{S}_{\mathrm{E}}^{'} = (E_x^{'}, E_y^{'})$ through an instrument is

$$\boldsymbol{S}_{\mathrm{E}}^{'} = \mathbf{J}\mathbf{R}_{\mathrm{E}}(\phi)\boldsymbol{S}_{\mathrm{E}}, \qquad (1)$$

where $\mathbf{J}$, which is typically called Jones matrix, is the instrumental response, and

$$\mathbf{R}_{\mathrm{E}}(\phi) = \begin{pmatrix} \cos\phi & \sin\phi \\ -\sin\phi & \cos\phi \end{pmatrix} \qquad (2)$$

is the relative rotation between the sky and the receptor by a parallactic angle ϕ. If we transform Eqn. (1) into the basis of Stokes parameters, we get

$$\boldsymbol{S}_{\mathrm{sp}}^{'} = \mathbf{M}\mathbf{R}(\phi)\boldsymbol{S}_{\mathrm{sp}}, \qquad (3)$$

where $\boldsymbol{S}_{\mathrm{sp}}$ is a 4-vector representing Stokes (I, Q, U, V), $\mathbf{M}$ the 4×4 Mueller matrix, and

$$\mathbf{R} = \begin{pmatrix} 1 & 0 & 0 & 0 \\ 0 & \cos 2\phi & \sin 2\phi & 0 \\ 0 & -\sin 2\phi & \cos 2\phi & 0 \\ 0 & 0 & 0 & 1 \end{pmatrix}. \qquad (4)$$

Note the relation between the 2-vector $\boldsymbol{S}_{\mathrm{E}}$ and 4-vector $\boldsymbol{S}_{\mathrm{sp}}$ is

$$\boldsymbol{S}_{\mathrm{sp}} = \mathbf{A}(\boldsymbol{S}_{\mathrm{E}} \otimes \boldsymbol{S}_{\mathrm{E}}^{*}), \qquad (5)$$

where $\otimes$ is Kronecker product and

$$\mathbf{A} = \begin{pmatrix} 1 & 0 & 0 & 1 \\ 1 & 0 & 0 & -1 \\ 0 & 1 & 1 & 0 \\ 0 & i & -i & 0 \end{pmatrix}. \qquad (6)$$

The relation between the Jones matrix $\mathbf{J}$ and Mueller matrix $\mathbf{M}$ is then

$$\mathbf{M} = \mathbf{A}(\mathbf{J} \otimes \mathbf{J}^*)\mathbf{A}^{-1}. \tag{7}$$

$\mathbf{J}$ can be parametrized as

$$\mathbf{J} = G\mathbf{\Gamma}(\gamma)\mathbf{R}_\Phi(\varphi)\mathbf{C}, \tag{8}$$

where G, the absolute gain, is a scalar. $\mathbf{\Gamma}(\gamma)$ is a matrix corresponding to the differential gain γ,

$$\mathbf{\Gamma}(\gamma) = \begin{pmatrix} e^\gamma & 0 \\ 0 & e^{-\gamma} \end{pmatrix}. \tag{9}$$

$\mathbf{R}_\Phi(\varphi)$ is a matrix corresponding to the differential phase φ,

$$\mathbf{R}_\Phi(\varphi) = \begin{pmatrix} e^{i\varphi} & 0 \\ 0 & e^{-i\varphi} \end{pmatrix}. \tag{10}$$

$\mathbf{C}$ is a matrix that represents a receiver with non-orthogonal receptors,

$$\mathbf{C} = \delta_\mathbf{0}\mathbf{L}(\theta_0, \epsilon_0) + \delta_\mathbf{1}\mathbf{L}(\theta_1, \epsilon_1), \tag{11}$$

where $\mathbf{L}(\theta, \epsilon)$ is written as

$$\mathbf{L}(\theta, \epsilon) = \begin{pmatrix} \cos\epsilon & i\sin\epsilon \\ i\sin\epsilon & \cos\epsilon \end{pmatrix} \begin{pmatrix} \cos\theta & \sin\theta \\ -\sin\theta & \cos\theta \end{pmatrix}. \tag{12}$$

ϵ and θ are the ellipticity and orientation of the receptor, respectively. $\delta_\mathbf{a}$ is the selection matrix,

$$\delta_\mathbf{a} = \begin{pmatrix} \delta_{0a} & 0 \\ 0 & \delta_{1a} \end{pmatrix}, \tag{13}$$

where δ_{ab} is the Kronecker delta.

$\mathbf{C}$ can be decomposed as

$$\mathbf{C}(\epsilon_0, \theta_0, \epsilon_1, \theta_1) = \mathbf{C}(\epsilon_0, \theta_0 - \phi_0, \epsilon_1, \theta_1 - \phi_0)\mathbf{R}_\mathrm{E}(\phi_0), \tag{14}$$

where

$$\mathbf{R}_\mathrm{E}(\phi_0) = \begin{pmatrix} \cos\phi_0 & \sin\phi_0 \\ -\sin\phi_0 & \cos\phi_0 \end{pmatrix} \tag{15}$$

is equivalent to the parallactic angle rotation. Therefore, one can define $\theta_+ \equiv \theta_0 + \theta_1$ and $\theta_- \equiv \theta_0 - \theta_1$ to separate the overall rotation from the relative rotation between receptors, and merge θ_+ into parallactic angle rotation.

Then one can transform $\mathbf{J}$ to Mueller matrix $\mathbf{M}$ with Eqn. (7).

To illustrate some of the structure of the Jones and Mueller matrices, we set $(\theta_0, \theta_1, \epsilon_0, \epsilon_1) = 0$, Eqn. (8) can be rewritten as:

$$\mathbf{J} = G\begin{pmatrix} e^{\gamma + i\varphi} & 0 \\ 0 & e^{-\gamma - i\varphi} \end{pmatrix}, \tag{16}$$

and the Mueller matrix becomes

$$\mathbf{M_0} = G^2 \begin{pmatrix} \cosh(2\gamma) & \sinh(2\gamma) & 0 & 0 \\ \sinh(2\gamma) & \cosh(2\gamma) & 0 & 0 \\ 0 & 0 & \cos 2\varphi & \sin 2\varphi \\ 0 & 0 & -\sin 2\varphi & \cos 2\varphi \end{pmatrix}. \tag{17}$$

In summary, the Jones matrix is a 2×2 complex matrix, in principle it has eight degrees of freedom. However, from Eqn. (7), one can see that the absolute phase of $\mathbf{J}$ does not affect the Mueller matrix $\mathbf{M}$. Therefore, the complete Jones/Mueller matrix model can be described

by seven parameters, which are the absolute gain G, the differential gain γ, the differential phase φ, θ_0, θ_1 the orientation of the two receptors, and the ellipticity of the receptors ϵ_0, ϵ_1.

3.2. Polarization calibration with pulsar
3.2.1. Solving Mueller matrix with Pulsar data

One can observe a polarized source, such as a pulsar, to measure $\boldsymbol{S}'_\mathrm{E}$ at parallactic angle ϕ. With data taken at several parallactic angles, one will have a set of simultaneous equations, $\boldsymbol{S}'_{\mathrm{E}i} = \mathbf{J}\mathbf{R}_\mathrm{E}(\phi_i)\boldsymbol{S}_\mathrm{E}$, or

$$\boldsymbol{S}'_{\mathrm{sp}i} = \mathbf{M}\mathbf{R}(\phi_i)\boldsymbol{S}_\mathrm{sp} \tag{18}$$

in the Stokes parameter basis. i indexes the observation at parallactic angle ϕ_i

Before solving for both the incoming signals of the pulsar and the Jones matrix parameters using these equations, we have to deal with two degeneracies: One of the degeneracies is between the Stokes parameters I and V of the incoming signal, and the other is between Stokes Q and U.

The degeneracies arise from the following: In Eqn. (18), one can equally substitute $\mathbf{M}$ and $\boldsymbol{S}_\mathrm{sp}$ with $\mathbf{M}\mathbf{D}^{-1}$ and $\mathbf{D}\boldsymbol{S}_\mathrm{sp}$, respectively, as long as the matrix $\mathbf{D}$ commutes with $\mathbf{R}$. In other words, if $\boldsymbol{S}_\mathrm{sp}$ is one solution of Eqn. (18), $\mathbf{D}\boldsymbol{S}_\mathrm{sp}$ will be another solution as well. In fact, any matrix $\mathbf{D}$ of the following form,

$$\mathbf{D} = a\begin{pmatrix} 1 & 0 & 0 & V_1 \\ 0 & 1 & 0 & 0 \\ 0 & 0 & 1 & 0 \\ V_2 & 0 & 0 & 1 \end{pmatrix} + b\begin{pmatrix} 1 & 0 & 0 & 0 \\ 0 & \cos\theta & \sin\theta & 0 \\ 0 & -\sin\theta & \cos\theta & 0 \\ 0 & 0 & 0 & 1 \end{pmatrix}, \tag{19}$$

will commute with $\mathbf{R}$ (see Appendix B of van Straten (2004)). The first term of Eqn. (19) corresponds to degeneracy between I and V, and the second term degeneracy between Q and U.

One way to break the degeneracy between Stokes I and V is to observe a standard calibrator with a known ratio of Stokes I to V. There is a built-in noise diode at the GBT that can serve this function. Ideally, the noise diode will produce pure linearly polarized signals at a position angle 45° to the two orthogonal receptors. We can therefore break the degeneracy between Stokes I and V by assuming that the noise diode produces no circular polarization signals. Alternatively, we can assume the system circular polarization V to be negligible while observing astrophysical calibrators.

As is the standard procedure, by taking the differences of on- and off-source observations of a standard calibrator, such as 3C295, one can estimate its circular polarization. One can therefore break the degeneracy by assuming the Stokes V of standard calibrators, which are reported to have a negligible level of V, to be zero.

The degeneracy between Q and U, which makes it impossible to calibrate absolute polarization angles on the sky without an external reference, is related to the definition of angles. Here we set the orientation of the first receptor by fixing $\theta_0 = 0$. Therefore, $\theta_- = -\theta_1$ in the following sections.

PSRCHIVE solves $\mathbf{J}$ by using a least-squares minimization method for each frequency channel (see van Straten

(2004) for more detail). It automatically selects several pulsar pulse phase bins, from pulsar data taken at different parallactic angles, to solve for the model parameters. The unknown variables are the Stokes parameters of the incoming pulsar signals and the Jones matrix parameters of the instrument. Because the total flux density I of pulsars typically varies on a time-scale of minutes, PSRCHIVE normalizes the Stokes parameters by the invariant interval $S = I^2 - Q^2 - U^2 - V^2$ instead (details in van Straten (2004)). We can therefore compare pulsar Stokes parameters between different scans.

However, the PSRCHIVE does not directly assume the circular polarization of the standard candle to be zero. Instead, PSRCHIVE provides two options: either assume the V of system temperature while directing the telescope to a standard candle , or the V of noise diode, to be zero. Following van Straten (2004), who suggests that the circular polarization of a noise diode is significantly different from zero, we choose the first option.

With pulsar observations at five different parallactic angles, we have 20 measurements (4 polarizations $\times$ 5 parallactic angles) at each frequency channel and each selected pulse phase bin. In addition to the flux calibrator data from quasar observations (four polarizations) and the noise diode data (four polarizations), we have 328 measurements for 16 selected pulse phase bins at each frequency channel. The number of variables at each frequency is 76, including a total of 64 Stokes parameters of the pulsar for the 16 selected pulse phase bins, six Stokes parameters of the flux calibrator and noise diode (the I of flux calibrator is assumed to be known, and the V of flux calibrator is set to be zero), and six instrumental Jones/Mueller matrix model parameters (i.e., the seven parameters describe in Section 3.1 except for θ_0, which is set to be 0 to break the degeneracy between Q and U). Once PSRCHIVE obtains the best fit instrumental parameters, it generates both the Jones matrix and Mueller matrix for each frequency channel with the formalism described in the above section.

Figures 1 and 2 show the Jones matrix obtained from pulsar data, where we took five five-minute tracking scans for pulsar B1133+16 in Jan, 2014 at different parallactic angles with the GBT. The standard candle used is quasar 3C295, which is known to be an unpolarized source at 800 MHz. The model parameters shown in Figure 2 are consistent with the ones shown by Han et al. (2009) in the overall.

3.2.2. *Determining parameters with noise diode*

We find that at the GBT, the value of φ changes dramatically day by day and needs to be determined with each observation; the values of G and γ are also found to change slightly day by day and significantly several times in a observing semester over six months.

Since at the GBT, the noise diode signal is injected into the receiver only after the separation of orthogonal polarizations, parameters $\epsilon_{0,1}$ and $\theta_{0,1}$, which describe the cross-talk between orthogonal polarizations, are expected to be negligible for noise diode signal. The Mueller matrix that applies to the noise diode signal can thus be written as Eqn. (17).

One can therefore solve for G, γ, and φ by inserting a known noise diode standard profile $\boldsymbol{S}_{\mathrm{ncal}}$ and the ob-
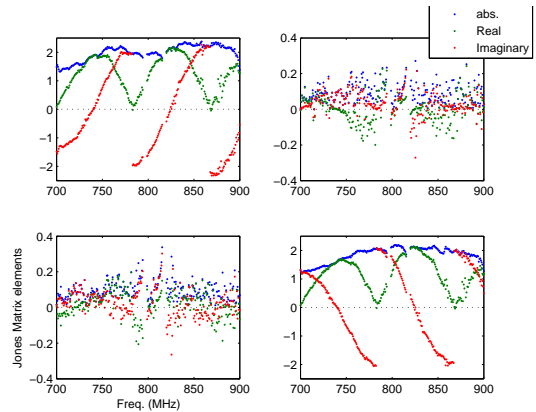

FIG. 1.— The Jones matrix elements of GBT as a function of frequency. The upper left is $\mathbf{J}(0,0)$, upper right $\mathbf{J}(0,1)$, lower left $\mathbf{J}(1,0)$, and lower right $\mathbf{J}(1,1)$. The Jones matrix is obtained from B1133+16 data. The unit is arbitrary. The features nears frequencies 800 MHz and 820 MHz are due to the resonance in the orthomode transducer (OMT) in this band at the GBT, and are excluded from all analysis in this paper.
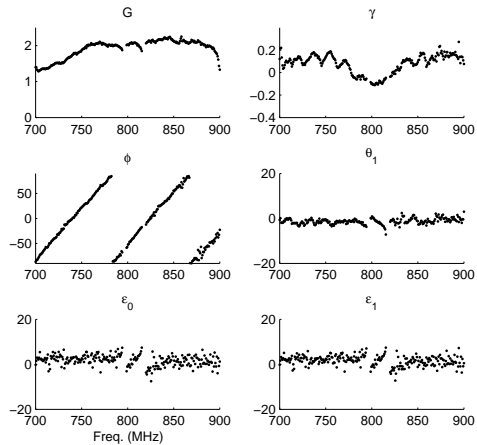

FIG. 2.— The values of Jones matrix parameters of GBT as a function of frequency. The parameters are obtained from B1133+16 data. The unit of G is abitrary, γ is dimensionless. φ, θ_1, ϵ_0, and ϵ_1 are in units of degree.

served noise diode data $\boldsymbol{S}'_{\mathrm{ncal}}$ into

$$\mathbf{M_0}\boldsymbol{S}_{\mathrm{ncal}} = \boldsymbol{S}'_{\mathrm{ncal}}. \qquad (20)$$

Assuming the noise diode frequency profile is stable over a few months, we can use the noise diode data calibrated by PSRCHIVE as the standard profile to solve for G, γ, and φ for each observation session. Combining these parameters with θ_1, ϵ_0, and ϵ_1 obtained from multiple parallactic-angle tracking scans of B1133+16, we can achieve $\sim 1.3\%$ accuracy on all the Stokes parameters, with respect to total intensity, of the unpolarized quasar 3C147. The accuracy of 1.3% is the RMS fluctuation of dozens of calibrated tracking scans on 3C147 over an entire semester.

3.3. *Parameter modification with Quasar data*
3.3.1. *Previous Assumptions*

The calibration method described above is based on the following assumption: The linear polarization frac-

tion, angle, and the circular polarization fraction of the target pulsar are assumed to be stable over the observation period, which is about six hours. To test the first assumption, we examine the calibrated pulsar properties as a function of time. Figure 3 shows the RMS of linear polarization fraction over five calibrated pulsar tracking scans taken in the same night. We find that the RMS fluctuation of the linear polarization fraction measured over multiple parallactic-angle pulsar tracking scans is higher than the thermal noise level. It appears the polarization fraction of pulsars is not stable enough for our purpose. The RMS fluctuation of the linear polarization angle ($\approx 2°$-$4°$) and circular polarization fraction ($\approx 1\%$-3%) are also larger than acceptable.

Because it takes a good amount of observing time (including overhead) to conduct multiple parallactic angle pulsar tracking scans, during our HI intensity mapping observing campaign spread over a few semesters, we only take multiple parallactic-angle pulsar tracking scans once every several months. The stability of the noise diode profile becomes crucial. The stability is tested with observations of on- and off-source quasar tracking scans while blinking the thermal noise diode at 15.26 Hz in every observing session. Comparing data with and without a bright quasar in the center of the beam, and data with and without the noise diode signal, one can derive T_x and T_y, the injected noise diode temperature in the two polarization directions, given the known spectrum of the quasar. We find that the noise diode is not stable over a time span of six months either. Figure 4 shows noise diode temperature measured with scans on 3C48 in 2011. There appears to be a discontinuity in noise diode temperature at scan 22, below which the receptor X has a higher temperature than receptor Y but with a 2dB attenuation above 840 MHz. This discontinuity was observed between June 27, 2011 and July 17, 2011, which coincided with the maintenance activity at the GBT when the 800 MHz receiver was taken down from the prime focus. It is quite possible that the noise diode was reset when the receiver reinstalled. Therefore, we need to modify the method of estimating the Jones/Mueller matrix for the GBT.

3.3.2. Noise Diode Behavior

In order to reduce the impact of noise diode instability, we examine T_x and T_y as a function of time and frequency, derived from quasar tracking scans in each session, then group all sessions into subsets according to the shapes of the derived noise diode frequency profiles. In practice, the number of identified noise diode profile shapes in each semester varies between 1 to 9 for the five semesters from 2011 to 2015. We average the $T_x(\nu)$ and $T_y(\nu)$ profiles within each subset to obtain $\tilde{T}_{x,j}(\nu)$ and $\tilde{T}_{y,j}(\nu)$, where j indexes subsets. Then we normalize the profiles to $\left\langle \sqrt{\tilde{T}_{x,j}\tilde{T}_{y,j}} \right\rangle_\nu = 1$, averaging over all frequency channels. We further average $\left\langle \sqrt{T_x T_y} \right\rangle_\nu$ over all tracking scans within each session to get a normalization factor N_k for each session, where k indexes sessions. Finally we obtain estimated noise diode profile for each session as $N_k\tilde{T}_{x,j}$ and $N_k\tilde{T}_{y,j}$, then apply them to correct $\boldsymbol{S}_{\mathrm{ncal}}$ in Eqn. (20). In order to reduce the impact

of errors associated with the estimation of noise diode profiles, we only allow $\langle T_x T_y \rangle_\nu$ to vary between sessions, and fix the profile shape within each subset.

3.3.3. First-order Correction

Assuming $\theta_1, \epsilon_0, \epsilon_1 \ll 1$, to first-order approximation we can calculate the resulting calibration errors induced by errors in values of Jones matrix parameters using Eqn. (A1) and (A3). The formalism is described in detail in Appendix A. Figure 2 suggests that the assumption of small θ_1, ϵ_0, and ϵ_1 values is sound for the GBT. We can also define $\epsilon_+ \equiv \epsilon_0 + \epsilon_1$ and $\epsilon_- \equiv \epsilon_0 - \epsilon_1$, for they are directly associate with Q-V and I-V leakages, respectively (see Appendix A and Britton (2000)).

For an unpolarized source like quasar 3C295, one can apply $\boldsymbol{S}_{\mathbf{sp}} = [I, 0, 0, 0]$ to Eqn. (A1) and (A3), and get

$$\delta Q/I = -(2\delta\gamma \cos 2\phi - \delta\theta_- \sin 2\phi) \qquad (21)$$

and

$$\delta U/I = -\delta\theta_- \cos 2\phi - 2\delta\gamma \sin 2\phi. \qquad (22)$$

These equations predict a sinusoidal dependence of the calibrated Q and U on parallactic angles. The predicted sinusoidal pattern is shown as blue dots in Figure 5, which represent the Q and U values of 3C295 data calibrated with a Mueller matrix calculated from pulsar observations,

For an unpolarized source, the calibrated values of Q and U, which are otherwise expected to be zero with perfect polarization calibration, are denoted as δQ and δU. Substituting these values into Eqns. (21) and (22), we obtain the best-fit values of $\delta\gamma$ and $\delta\theta_-$.

As a consistency check, we calculate the values of $\delta\gamma$ and $\delta\theta_-$ with data on 3C147, adjust the γ and θ_- parameters accordingly and apply them to the polarization calibration of 3C295 data. The 3C295 data calibrated with the modified parameters are shown as green and red dots in Figure 5. Modification of γ and θ_- dramatically reduce the fluctuation of calibrated Q and U of 3C295. This implies the modification of γ and θ_- parameters is a sound approach.

On the other hand, the matrix element $(4, 1)$ in the right hand side of Eqn. (A3) describes the leakage from I into V due to $\delta\epsilon_-$. The circular polarization level of 3C295 is smaller than 0.6% at our frequency band, thus we assume that the oscillating pattern of V of calibrated 3C295 data, which is shown as the blue curve in Figure 6, is caused by $\delta\epsilon_-$ in the parameter set we applied. Just as for $\delta\theta_-$ and $\delta\gamma$, we also use a modified ϵ_- derived from 3C147 data to calibrate 3C295 data. The corrected V of 3C295 is much closer to zero as shown by the green curve in Figure 6.

Once we obtain the modified γ, θ_-, and ϵ_- from quasar data, one can apply the solutions to other quasars including 3C48, 3C295, 3C147, and 3C286. The RMS of calibrated stokes parameters over dozens of tracking scans through an entire observing semester are about 0.6%-0.8% of the quasar intensity in most of the frequency channels. 3C286, a slightly polarized quasar, is taken as an example to illustrate the outcome of the parameter correction, indicated by the blue and green lines in Figure 7.

The modified θ_- can be used to test the assumption that the cross talk between T_x and T_y of the noise diode

is negligible. As shown in Eqn. (A2), θ_- describes the leakage between I and U. The θ_- experienced by the sky signal can be approximated as a linear combination of θ_- before and after noise diode signal injection. We denote the latter one as $\theta_{-,\mathrm{ncal}}$ because it is the $\theta-$ which noise diode signal experienced. As U_{ncal} is strong ($\approx 80\%$ of I_{ncal}), fluctuations in $\theta_{-,\mathrm{ncal}}$ will contribute to the fluctuations in I_{ncal}. Therefore, we postulate that the measured I_{ncal} is to correlate with the θ_- value estimated from quasar data, if the fluctuation of $\theta_{-,\mathrm{ncal}}$ is not negligible.

We therefore correlate fluctuations over time and frequency channels of I_{ncal} and θ_- obtained from quasar 3C48 taken in 2014 and 2015. The most prominent patterns extracted using singular-value decomposition in frequency-time space are removed before correlation. These removed patterns of I_{ncal} and θ_- do not correlate with each other. On the other hand, from previous noise diode data, we found that $T_{x,\mathrm{ncal}}$ and $T_{y,\mathrm{ncal}}$ tend to preserve spectral shape over several nights with normalization changes each night. This kind of pattern matches what we get in the first SVD mode. These two facts imply that these removed modes can be considered to represent fluctuations of I_{ncal} and θ_- before the light path of sky signal merge with the noise diode signal. The residual I_{ncal} and θ_- have a correlation coefficient of $r = 0.24 \pm 0.03$, significantly different from 0. As a sanity check, we remove the correlated part from I_{ncal}, and find the RMS of measured I_{ncal} only reduced by $\approx 0.04\%$ of total I_{ncal}. Although there is statistically significant correlation between residual I_{ncal} and θ_-, the impact of this correlation is much smaller than the uncertainty level, 0.6%-0.8%, of our calibration. We perform a similar check on ϵ_- and noise diode V_{ncal}, for $\delta\epsilon_-$ would results in leakage from I_{ncal} into V_{ncal} if $\delta\epsilon_-$ happens after noise diode signal injecting into the receiver. We do not find significant correlation between ϵ_- and the V_{ncal}. We therefore conclude that the cross talk between $T_{x,\mathrm{ncal}}$ and $T_{y,\mathrm{ncal}}$ is negligible.

3.4. *Ionospheric Rotation Measure Correction*

Ionospheric Faraday rotation is another effect that needs to be accounted for in the data. Faraday rotation is the rotation of linear polarization direction when photons propagate through magnetized free electrons. The angle of rotation is proportional to the wavelength λ of light as λ^2, and can be written as $\theta_{\mathrm{FR}} = \phi_{\mathrm{RM}}\lambda^2$, where ϕ_{RM} is Rotation Measure (RM). RM can be calculated as

$$\phi_{\mathrm{RM}} \approx (2.62 \times 10^{-13}\mathrm{T}^{-1}) \int n_{\mathrm{e}}(s)B_{\parallel}(s)ds, \qquad (23)$$

where n_{e} is free electron density, $B_{\parallel}$ is the strength of magnetic field component parallel to the line of sight, T stands for Tesla, the SI unit magnetic field strength, and ds is integrated along the line of sight.

Photons from astronomical sources propagate through the terrestrial ionosphere, composed of the free electrons magnetized by the geomagnetic field, the linear polarization angle of light is thus rotated by the Faraday effect. The RM depends on the spatial distribution of n_e, which is a function of time, and the trajectory of light propagation, which is determined by azimuth and elevation of the

pointing of the telescope. We adopt empirical orthonormal functions (EOFs)(Fuller-Rowell et al. 2006) and incorporate ionospheric information released by US-TEC (Fuller-Rowell et al. (2006) and Araujo-Pradere et al. (2007)) to estimate free electron density at the time of observation. The geomagnetic field is calculated using the International Geomagnetic Reference Field (IGRF) (Finlay et al. 2010). After applying the free electron number density and geomagnetic field to Eqn. (23), we obtain the RM values and calculate θ_{FR} caused by ionospheric free electrons. Faraday rotation can be corrected by simply adding θ_{FR} to the parallactic rotation angle ϕ in Eqn. (4).

With $\phi_{\mathrm{RM}} = 2m^{-2}$, which is a typical ionospheric ϕ_{RM} value at the GBT site during night time when we observe, θ_{FR} is 12.7° at 900 MHz and 21.0° at 700 MHz. The ionospheric Faraday rotation affects the linear polarization direction rather significantly in our observing frequency range.

Figure 8 shows the comparison of RM values fitted as the slope of linear polarization angles with respect to λ^2 using calibrated 3C286 data, the phase angles of calibrated 3C286 data averaged over frequency channels, and estimated ionospheric RM. The right panel of Figure 8 shows that our RM correction effectively reduces the fluctuation of polarization angle over time.

In principle, the remaining RM after ionospheric RM correction should be the RM of the celestial object. However, it is reported that the RM of 3C286 is very close to zero (Perley and Butler 2013), which significantly differs from what we measure in Figure 8. Note though that the FWHM of the GBT beam in our frequency band is about $15' - 19'$, the on-source 3C286 data will thus include contributions from the surrounding Galactic Foreground. Although we subtract off-source data, which is taken 3 degrees away from 3C286, the Galactic foreground at these two patches may differ and affect the estimated RM value.

We have therefore taken 33 tracking scans of pulsar B1929+10. We eliminate Galactic foreground RM contribution by gating the pulsar and subtracting off-pulse from on-pulse data, and expect the pulsar RM measurement to be free of Galactic foreground contamination. After ionospheric RM correction, the pulsar RM calculated from the slope of $arg(Q + iU)$ changes from $-5.9 \pm 0.3m^{-2}$ to $-7.1 \pm 0.3m^{-2}$, which is consistent with the RM value from the literature, $-6.9m^{-2}$ (Johnston et al. 2005). We therefore validate our ionospheric RM correction procedure.

4. POLARIZED BEAM RESPONSE

In the previous section we have focused on on-axis (boresight) polarization calibration only. However, off-axis polarization leakage can potentially contaminate HI intensity maps and power spectrum estimation. Considering the full polarized beam response, Eqn. (3) should be rewritten as a convolution,

$$\boldsymbol{S'}(\vec{x}) = \int \mathbf{M}(\Delta\vec{x})\mathbf{R}(\phi)\boldsymbol{S}(\vec{x'})d^2x', \qquad (24)$$

where $\vec{x}$ and $\vec{x'}$ are the two-dimensional positions in the sky, $\Delta\vec{x} = \vec{x'} - \vec{x}$. $\vec{x}$ and $\vec{x'}$ are defined in horizontal coordinate system. $\vec{x}$ is the position of the boresight
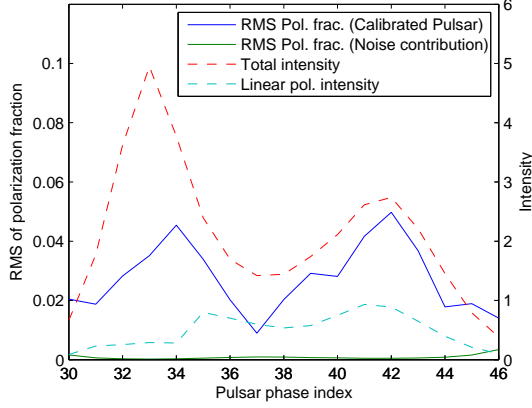
FIG. 3.— The RMS of linear polarization fraction of pulsar B1133+16. The X axis is pulsar phase index. The blue curve is derived by comparing 5 tracking scans on B1133+16 taken at the same night. The green curve shows the contribution of noise. The dashed lines show the total and linear polarization intensity of the pulsar. The unit of intensities is arbitrarily.
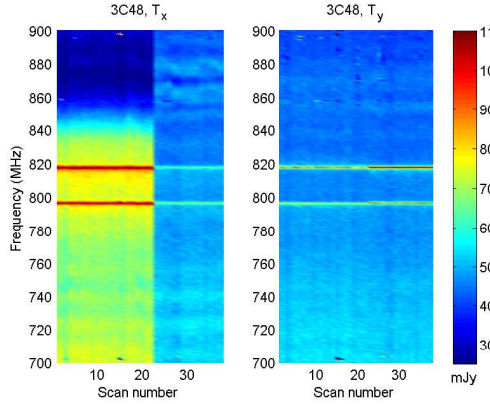

FIG. 4.— An example of instability of GBT noise diode. In this figure we show the T_x and T_y of noise diode derived by comparing noise diode data with 3C48 data, which were taken at the same time. The left panel and right panel are T_x and T_y of noise diode, respectively. The intensity unit here is mJy. The dataset shown here consists 38 tracking scans spreading from May to August, 2011. The two horizontal stripes at frequencies near 800 MHz and 820 MHz correspond to bad channels due to the resonance in the orthomode transducer (OMT) in this band at the GBT, and are excluded from all analysis.

and $\vec{x'}$ the position of the source on the sky, so that $\Delta\vec{x}$ represents the source position relative to the boresight on the sky. In the case of a point source, where $\boldsymbol{S}(\vec{x'}) = \boldsymbol{S_0}\delta(\vec{x'} - \vec{x_0})$, Eqn. (24) reduces to Eqn. (3) with $\mathbf{M} = \mathbf{M}(\vec{x_0} - \vec{x})$. In this section we use quasars and pulsars as probes to investigate the feature of $\mathbf{M}(\Delta\vec{x})$. We also discuss the advantages and weaknesses of these two types of targets for polarization calibration.

4.1. *Polarized Beam from Quasar spider scans*
4.1.1. *Polarized Beam Pattern*

We perform the so-called 'spider scans' on unpolarized quasars to investigate the structure of the first column of the Mueller matrix $\mathbf{M}(\Delta\vec{x})$, i.e., the leakage contributions from intensity to polarization. To conduct a spider scan, we slew the telescope along four $1°$ paths across the central source: one of the four paths is iso-azimuthal,
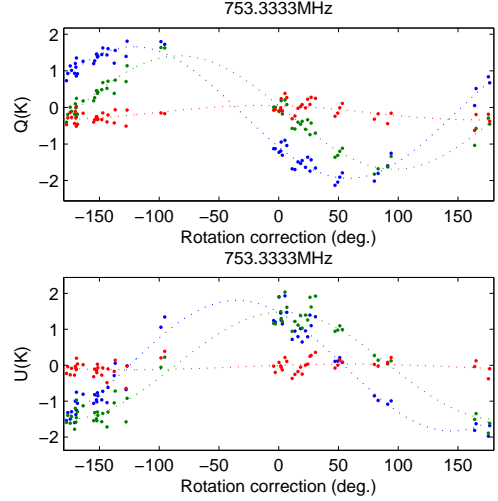

FIG. 5.— Comparison of calibrated Q (upper) and U (lower) of an unpolarized source 3C295 with/without parameter modifications. The blue dots show the data calibrated by the method described in Section 3.2, the green dots are calibrated with modified γ, and the red ones are calibrated with modified γ and θ_-. Each dot corresponds to one 1-minute tracking on 3C295. The parameter modification is described in Section 3.3.3. The rotation correction here is defined as 2ϕ. The total intensity of 3C295 in frequency range 700 - 900 MHz spread from 58 K to 72 K.
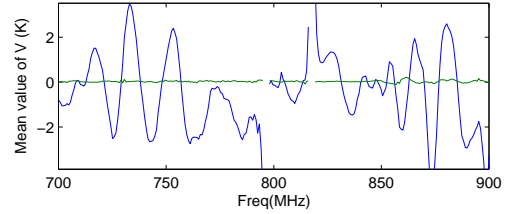

FIG. 6.— Calibrated V of 3C295. The blue curve shows the calibrated V from pulsar tracking scans, and the green curve includes the ϵ_- correction with data from 3C147, which helps substantially in achieving $V \sim 0$. The total intensity of 3C295 in frequency range 700 - 900 MHz spread from 58 K to 72 K.

one iso-elevation, and the other two are $45°$ from the first two (shown as black lines in the upper panels of Figure 9). The lengths of the paths are 4.0 and 3.2 times of the beam FWHM at 900 MHz and 700 MHz, respectively. We select a few unpolarized quasars, including 3C48, 3C295, and 3C147, as targets. The upper panels of Figure 9 show the beam maps from direct interpolation of 3C295 spider scans at a single frequency channel. The data shown in Figure 9 have been calibrated with the boresight calibration method described in Section 3.

In order to quantify the resulted polarization beams and minimize the impact of observational noise, we model the spider scan maps with the two-dimensional Gauss-Hermite functions, which are perturbations around a two-dimensional Gaussian profile. The 2D Gauss-Hermite function is written as

$$\mu_{ij}\left(\frac{x}{x_0}, \frac{y}{y_0}\right) = e^{\frac{-(x^2+y^2)}{2\sigma^2}} H_i\left(\frac{x}{x_0}\right) H_j\left(\frac{y}{y_0}\right), \quad (25)$$

where the σ is the beam size, H the Hermite polynomials, x_0 and y_0 are characteristic scales in the x and y directions.
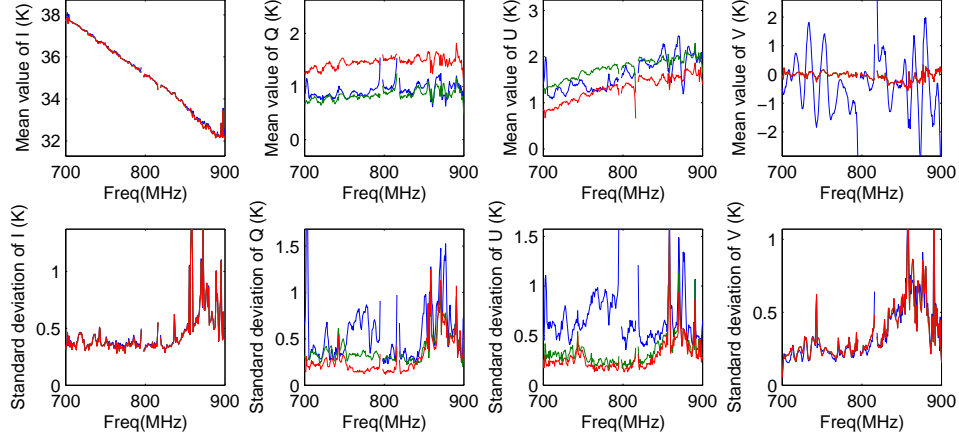
FIG. 7.— Calibrated 3C286 data. The upper panels show calibrated Stokes parameters averaged over 57 tracking scans on 3C286, while the lower ones show the standard deviations between those tracking scans. The blue lines show the result of calibration with parameters solved from pulsar data, the green lines correspond to calibration with modified θ_- and ϵ_- (based on 3C48 data), and the calibration shown as red lines using exactly same parameters except additional ionospheric Rotation Measure correction.
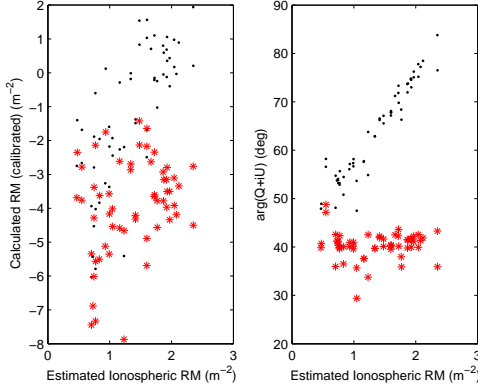
FIG. 8.— Comparison of linear polarization angle of 3C286 with (red asterisks) and without (black dots) ionospheric RM correction. The left panel shows the RM values fitted as the slope of linear polarization angles with respect to λ^2 using calibrated 3C286 data. The right panel are the phase angles of calibrated $Q + iU$ averaged over frequency channels. The x-axes are ionospheric RM values estimated with US-TEC model. The correlation coefficient r between x-axis and y-axis values of black dots, which show the results before RM correction, is 0.73 in the left panel and 0.95 in the right one. The correlation coefficients become 0.29 and 0.02, respectively, after applying RM correction. As shown here, the RM correction significantly reduces the variance and the averaged values of polarization angles of 3C286.

The Gauss-Hermite fit is then

$$S_{(I,Q,U,V)}(x,y) = \sum_{i=0}^{n} \sum_{j=0}^{n} a_{(I,Q,U,V),ij} \mu_{ij} \left(\frac{x}{x_0}, \frac{y}{y_0} \right), \quad (26)$$

where $a_{(I,Q,U,V),ij}$ are fitting coefficients.

We choose $n = 2$ to avoid over-fitting. σ is set to be the best-fit Gaussian beam size σ_g of I, and $x_0 = y_0 = \sigma_g$. The lower panels of Figure 9 show the best fit $S_{I,Q,U,V}$.

The most prominent feature of the derived polarized beam patterns is the dipole shape of the Stokes V beam. The dipole peak and trough are $\approx 12\%$ of the intensity at beam center. The dipole pattern in V is expected due to the off-axis design of the GBT (Srikanth 2012).

4.1.2. Q-V and U-V coupling

We further discover that the derived Q and U beam patterns show similar dipole shapes as the V beam, albeit at a lower level. Eqn. (A2) indicates that the errors in ϵ_+ and φ may induce leakage from V to Q and U, respectively. Eqn. (A2) also implies that ϵ_+ and φ are not easy to be constrained solely from unpolarized sources because these two parameters are absent in the first column of the first order approximation of δM, which describes the response of an unpolarized source. Therefore, we suspect that the Q and U beam dipole patterns may be due to leakage from the dipole pattern of V into Q/U, introduced by imperfect ϵ_+ and φ parameters we use in the boresight calibration stage, as described in Section 4.1.1

We quantify the Q-V and U-V linear correlations below to test this hypothesis. We fit a linear regression model to the calibration spider scan data in the form of $Q(x,y) + iU(x,y) = c + \tau V(x,y) + r(x,y)$, where c and τ are a constant and the complex linear coefficients, respectively, and r the residual. τ describes the leakage fraction, $\tau = \delta M_{2,4} + i\delta M_{3,4}$ in Eqn. (A2). The blue and green lines in Figure 10 show the real and imaginary part of τ, respectively.

4.1.3. U-V Correction

These relations could be intrinsic. They could also come from inappropriate polarization calibration. The red line in Figure 10 indicates the assumed argument of $(U_{\text{ncal}} + iV_{\text{ncal}})$ derived from the noise diode Stokes parameters yielded by the analysis of the pulsar observations using the PSRCHIVE tools. There is a strong correlation between the slope of the linear U-V relation (the imaginary part of τ) and the PSRCHIVE-derived noise diode argument.

As discussed in Section 3.2, we assume a noise diode frequency profile $\mathbf{S}_{\text{ncal}}(\nu)$ to solve for G, γ, and φ for each observing session. Looking at the third and fourth rows of Eqn. (20), it can be shown that $\varphi = 0.5 \times \arg[(U'_{\text{ncal}} + iV'_{\text{ncal}})/(U_{\text{ncal}} + iV_{\text{ncal}})]$. Combined with Eqn. (A2), one can see that a biased $\delta \arg(U_{\text{ncal}} + iV_{\text{ncal}})$ will lead to

a $\delta U = V \times \delta \arg(U_{\mathrm{ncal}} + iV_{\mathrm{ncal}})$. Therefore, the strong correlation between $\arg(U_{\mathrm{ncal}} + iV_{\mathrm{ncal}})$ and the imaginary part of τ implies that $\delta \arg(U_{\mathrm{ncal}} + iV_{\mathrm{ncal}})$ is responsible for the correlation between U and V. In fact, after setting $\arg(U_{\mathrm{ncal}} + iV_{\mathrm{ncal}}) = 0$, the correlation between the U and V beam disappears.

4.1.4. Q-V Correction

On the other hand, the Q-V relation could be also from errors in the derived Mueller matrix parameters. Assuming errors in ϵ_+ is the only source of the observed Q-V coupling in spider scan data, we estimate $\delta\epsilon_+$ from 3C295 spider scan data, and apply the 'corrected' ϵ_+ to spider scan data of other unpolarized sources, including 3C147 and 3C295. It appears that the dipole features in Q are removed by the correction of ϵ_+.

However, the removal of dipole shapes in Q does not answer the question: Does the dipole shape come from leakage of V to Q due to $\delta\epsilon_+$? Or is it an intrinsic beam feature? To distinguish these two possible scenarios, we apply the modified ϵ_+ to the polarized 3C286 data.

The linear polarization fraction of 3C286 is $\sim 5\%$, and the circular polarization is negligible. One can expect that $\delta\epsilon_+$ mainly influences V in the calibrated 3C286 data. Comparing the RMS of V over tracking scans with different parallactic and Faraday rotation angles, we may have a handle on the origin of the Q-V coupling.

We use 57 scans of 3C286 taken in 2011 to perform the test. The angles of rotation ϕ caused by sky rotation and ionospheric Faraday rotation range between $-88.4°$ to $60.6°$. We calculate $\sigma_V(\nu)$, the RMS of calibrated V over 57 tracking scans at each frequency channel, discard the highest 10% $\sigma_V(\nu)$ values to minimize impact of RFI and calculate the mean values. With ϵ_+ derived from pulsars and subsequently modified by spider scan data, the mean value of σ_V reduces from $0.752\% \pm 0.016\%$ to $0.716\% \pm 0.018\%$. The improvement appears marginal.

Figure 9 shows examples of the polarization beam pattern obtained from quasar spider scans, after correcting the φ and ϵ_+ parameters. In addition to the dipole pattern in the V beam, the Q and U beams show a less prominent quadrupole feature in the frequency range of 750-850 MHz. The amplitudes of these features are plotted as a function of frequency in Figure 11.

4.2. Polarization Beam from Pulsar tracking scans

Unpolarized quasar data provide useful information on the first column of $\mathbf{M}(\Delta\vec{x})$, and polarized sources are required in order to characterize the entire Mueller matrix. However, polarized quasars, such as 3C286 with a polarization fraction of about 5%, cannot provide significant signatures. For example, the expected leakage beam pattern from Q to I, according to the measured Mueller matrix model, is about 2%. With parallactic angle rotation, the change in Q of a 5% linearly polarized source is no greater than 10% of total intensity. The signature of Q leakage to I is therefore 0.2% at most, below our calibration significance of 0.6%. Furthermore, variations of the diffuse Galactic foreground radiation in the primary beam can contaminate the observation; it is difficult to completely separate quasar signals from the diffuse foreground, given a primary beam FWHM of 15' at 800 MHz at the GBT. We therefore solve for the full Mueller matrix parameters of the primary beam with off-source pulsar data; by subtracting off-pulse phase bins from the on-pulse data, we mitigate the diffuse background while preserving the pulsar signals.

Assuming a known pulsar profile, we solve for the full Mueller matrix with the primary beam pattern $\mathbf{M}(\Delta\vec{x})$ at discrete positions, $\vec{x_0}$, assuming $\boldsymbol{S}(\vec{x'})$ is a delta function peaking at $\vec{x_0}$ in Eqn. (3).

We take 59 tracking scans of pulsar B1133+16, including 27 on-source tracking scans, and 32 off-centered ones with positions spread within a $0.19°$ radius from the beam center. The radius of $0.19°$ is about 0.7 times the beam FWHM at 800 MHz. The B1133+16 pulsar profile is obtained from multiple parallactic angle observations as described in Section 3.2 and use PSRCHIVE matrix template matching mode described in van Straten (2006) and van Straten (2013) to solve for the Mueller matrix parameters for each on- and off-source tracking scan. We allow θ_0 to vary to account for possible relative Q-U rotation between beam center and other parts of the beam.

After solving the Mueller parameters at 33 locations (one on-source and 32 off-centered ones), we again perform a 2D Gauss-Hermite fit (Eqn. (25)) to model the beam. Due to observational noise and variations of the pulsar profile itself, we are not able to model at high confidence level the beam pattern for individual channels. Instead, we average the Mueller parameters over the frequency range 755-845 MHz for the Gauss-Hermite fitting.

Figure 12 shows the Mueller matrix beam calculated with best fit results of parameters. As 3C295 is unpolarized, the first column of Figure 12 correspond to spider scan results on 3C295. Comparing Figure 9 and Figure 12, we find similar beam patterns with leakage derived from pulsar data and quasar spider scans.

To verify the goodness of fit, we perform a 'significance test' on each Jones matrix parameter. We simulate 33 sets of Mueller parameters, each with a normal distribution and a zero mean, and randomly assign them to the 33 locations. We again perform the 2D Gauss-Hermite fits, and record $R^2 \equiv 1 - (\sigma_{\mathrm{residual}}/\sigma_{\mathrm{data}})^2$, where σ_{data} and $\sigma_{\mathrm{residual}}$ are the standard deviations of the 33 simulated input and fitted parameters, respectively. With 500 such simulations, we derive the probability $P(R^2)$ that random parameters get better fitting results. It appears only the ϵ_- fit, which describes the dominant Stokes I to V leakage, is significant ($P < 5\%$). Although γ and θ_- show similar patterns as Q and U, respectively, they do not pass the significance test.

According to the spider scans, the expected patterns of Stokes I leakage into Q and U are less than one sixth in amplitude of Stokes I leakage into V, and are comparable to the uncertainty of polarization fraction of pulsar B1133+16, as shown in Figure 3. Therefore, it is not entirely surprising that we cannot detect significant patterns of γ and θ_-. Pulsar B0450+55 also shows a similar level of fluctuations in polarization fraction, unfortunately.

5. PROCEDURE OF ON-AXIS POLARIZATION CALIBRATION

The essential task for on-axis polarization calibration in this work is determining the parameters G, γ, φ, θ_-,
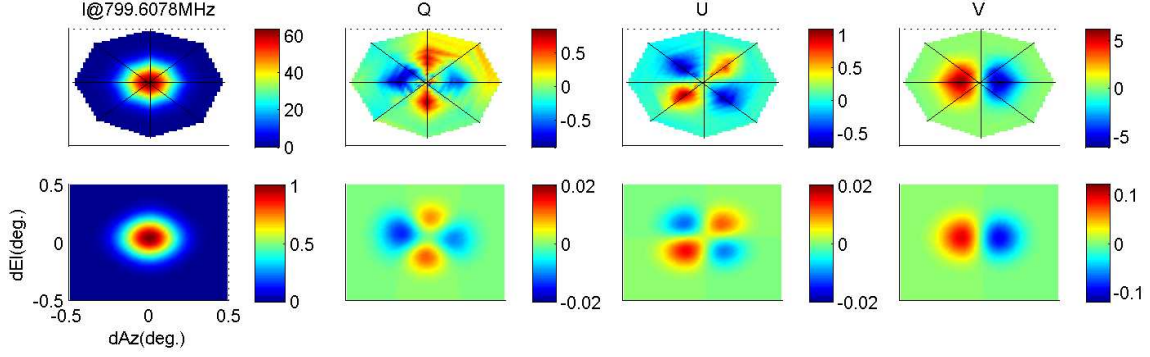
FIG. 9.— Polarized beam pattern at 800 MHz derived from spider scans of 3C295. The patterns in the upper panels are linear interpolation over the calibrated data of the spider scan, and the lower ones show the best fit results of the Gauss-Hermite model. The color scales of the upper panels are temperature in units of Kelvin, while the lower panels show fractional intensity compared to central source 3C295. Note we use modified Mueller matrix parameters as described in Section 4.1.2 and 4.1.4. As a result, the dipole patterns in the Q and U beams, first reported in Section 4.1.2, have been mitigated in this figure.
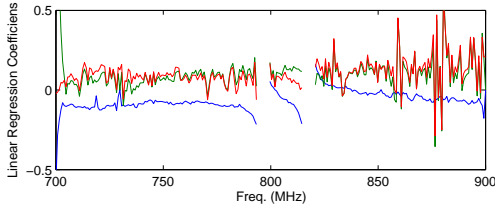
FIG. 10.— Q-V and U-V correlations in spider scan data. The blue and green lines show the real and imaginary part of τ. They also correspond to the Q-V and U-V correlations, respectively (see discussions in Section 4.1.2). The red line indicates the pre-assumed $\arg(U + iV)$ of the noise diode, which is used to calibrate φ for each night.
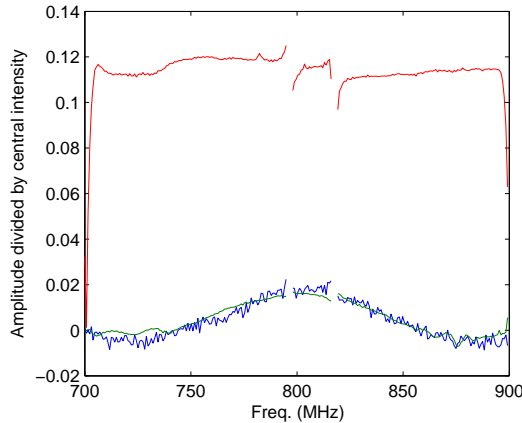

FIG. 11.— Coefficients of spider scan beam maps including quadrupole term of Q(blue), quadrupole term of U(green) and dipole term of V(red). The coefficients here are normalized by the peak value of I beam, and averaged over 7 spider scans on 3C48, 3C147, and 3C295.

ϵ_+ and ϵ_- as functions of time, and $\phi_{\rm RM}$ as function of time, azimuth, and elevation. Here we will summarize the methodology we adopt to determine these parameters.

1. Estimate noise diode frequency profile for each session with data of on/off source tracking scans on unpolarized quasars, like 3C48, 3C147, and 3C295 (Section 3.3.2).

2. Estimate G and γ by comparing observed noise diode data with estimated noise diode profile (Section 3.2.2).

3. Estimate φ from observed $\arg(U'_{\rm ncal} + iV'_{\rm ncal})$ of noise diode with assumed $V_{\rm ncal} = 0$ in real noise diode signal. (Section 4.1.3).

4. Apply G, γ, and φ to calibrate unpolarized quasar data (with the other parameters set to be 0). Then modify γ, θ_-, and ϵ_- based on quasar data calibrated in this step (Section 3.3.3).

5. Apply G, φ, along with modified γ, θ_-, and ϵ_- to calibrate spider scan data on another unpolarized quasar. Then estimate ϵ_+ with correlation between dipole features in Q and V data (Section 4.1.4).

6. Estimate $\phi_{\rm RM}$ with EOFs, US-TEC data, and IGRF. Then do ionospheric RM correction accordingly (Section 3.4).

6. DISCUSSION AND CONCLUSION

In this paper, we present the polarization calibration methodology for the GBT HI intensity mapping experiment. Accurate polarization calibration is critical to properly mitigate the unwanted leakage from polarized synchrotron foregrounds into total intensity.

We use multiple parallactic angle pulsar observations to solve for the six Jones Matrix parameters at boresight in each of the 256 frequency channels between 700-900 MHz at the GBT. Applying the solutions to unpolarized quasar observations, the RMS fluctuations of the Stokes parameters over time are about 1.3%-1.7% of total intensity. As a first-order correction, some of the Jones Matrix parameters are further modified based on tracking and spider scans of quasars. The RMS fluctuation reduces to 0.6%-0.8% of total intensity after the correction.

In Section 3.2 we discuss that there are two ways to break the degeneracy between I and V in PSRCHIVE: One assumes V to be negligible while observing a standard calibrator, i.e., the sum of V from the astrophysical calibrator, the (diffuse) sky, and the system, is negligible. However, the ϵ_- parameter obtained from PSRCHIVE
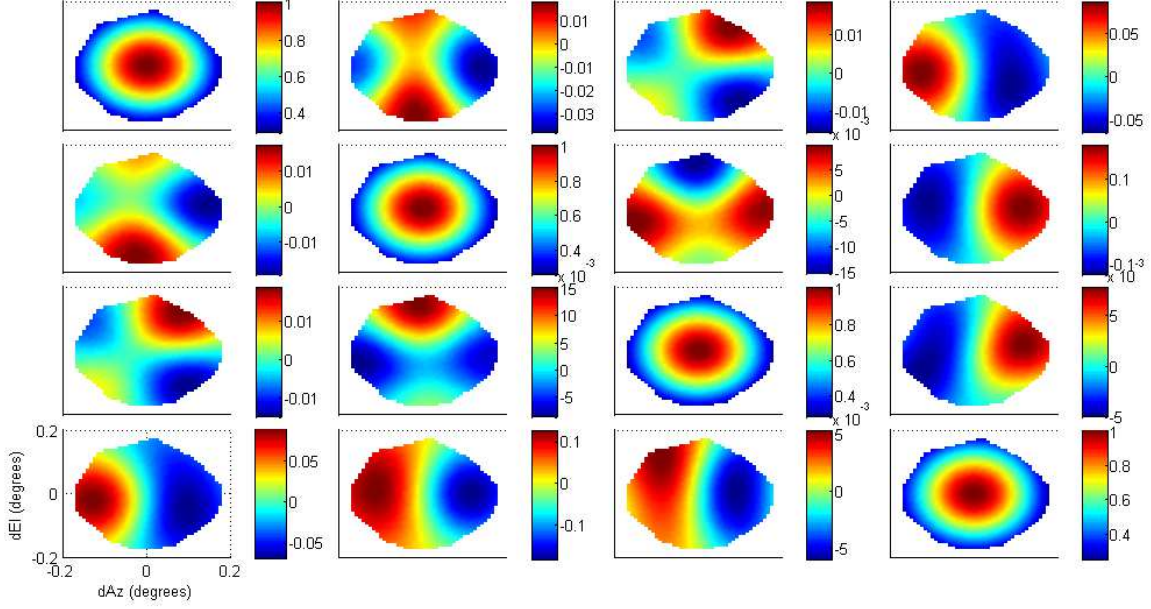
FIG. 12.— Beam pattern of the 4×4 Mueller matrix elements fitted with off-centered pulsar tracking scans. The diagonal elements are normalized to one, and from top-left to bottom-right the diagonal panels correspond to $M_{II}, M_{QQ}, M_{UU}, M_{VV}$, respectively.

under this assumption, which mainly describes the leakage between I and V, appears to be incorrect. This assumption does not seem to be valid in our case.

The other approach is to assume the V/U ratio of the noise diode is known. Section 4.1.2 and Figure 10 suggest that this could be a good assumption. However, PSRCHIVE assumes the noise diode signal is injected early in the system so that it shares the same light path as the sky signal; this is not the case for our GBT 800MHz observations, since the noise diode signal is injected after the OMT as discussed in Section 2.

Another explanation for the imperfection might be the variation of polarized pulsar profiles. PSR B1133+16, one of the pulsars we use to solve the Jones Matrix parameters, has been reported to have "orthogonally polarized modes", which may be responsible for the variations in the integrated fractional polarization and position angle of the pulsar (Karastergiou et al. 2002). The polarized pulse or frequency profiles of pulsars can in general fluctuate due to the astrophysical complexity of the pulse mechanism, or interference of the interstellar medium.

The polarized frequency profiles of quasars are more stable. However, with high fractional linear polarization and non-negligible circular polarization, pulsars provide more information needed to solve for all the Jones matrix model parameters than quasars, which are usually slightly or not polarized. Some of the parameters, including φ, ϵ_+, and θ_+, cannot be constrained by unpolarized sources. We can determine θ_+ by comparing the calibrated polarization position angle of 3C286 with the known value, while φ can be constrained by a highly polarized noise diode, which is however found to contain an uncertain V/U spectrum. The ϵ parameter is not affected by the noise diode as the signal injection takes place after the dipole receptor in the signal stream at the GBT.

Off-centered polarization leakage is also an important source of contamination. With quasar spider scans, we find a dominant dipole feature in the Stokes I to V leakage pattern, which is at the $\approx 12\%$ level, and secondary quadrupole features of Stokes I to Q and I to U leakage patterns, which are $\lesssim 2\%$ of total intensity. With the leakage of V dipole feature into Q and U, we can estimate $\delta\varphi$ and $\delta\epsilon_+$, and improve the calibration of polarized sources, like 3C286. Although there are still potential intrinsic dipole features in Q and U beam pattern which have yet to be separated from leakage of U.

We find similar features using off-centered pulsar observations and map out the entire Mueller matrix primary beam. However, the Stokes I to V leakage appears to be the only significantly determined beam pattern. The beam features of I leakage to Q and U are comparable to the variation of polarization profile of PSR B1133+16. Therefore, it is not surprising that we cannot significantly measure these features in the pulsar data.

In this paper, we measured the RMS fluctuations of calibrated on-source data of quasars, including unpolarized 3C48, 3C295, and 3C147, and slightly polarized 3C286, to be 0.6-0.8% of the total intensity. We also mapped the polarization beam pattern. Accurate polarization calibration at this level is required to mitigate the polarized foreground contribution for HI intensity mapping power spectrum measurements. We will report improvements on the redshifted HI power spectrum in future work. We will also investigate the Faraday rotation measure (RM) synthesis of Galactic foregrounds in the HI intensity mapping fields.

APPENDIX

FIRST-ORDER APPROXIMATION OF THE POLARIZATION CALIBRATION ERROR

In the model we use, $\mathbf{J}$ is a function of seven Jones matrix parameters, which can be rewritten as $\mathbf{J}(\vec{p})$, where $\vec{p} = \{p_i\} = \{G, \gamma, \varphi, \theta_+, \theta_-, \epsilon_+, \epsilon_-\}$ is the parameter vector. ϵ_+ and ϵ_- are defined as $\epsilon_+ = \epsilon_0 + \epsilon_1$ and $\epsilon_- = \epsilon_0 - \epsilon_1$. Mueller matrix can also be written as a function of these parameters $\mathbf{M}(\vec{p})$. See Section 3.1 for details.

Ideally, the polarization calibration should recover the real signal by applying inverse matrices of $\mathbf{M}$ and $\mathbf{R}(\phi)$ to Eqn. (3). However, if the estimated parameter vector $\vec{p'} = \vec{p} + \delta\vec{p}$ is slightly different from real parameter vector $\vec{p}$, the calibration procedure becomes

$$
\begin{aligned}
\boldsymbol{S}''_{\mathrm{sp}} &= \mathbf{R}^{-1}\mathbf{M}(\vec{p'})^{-1}\boldsymbol{S}'_{\mathrm{sp}} \\
&= \mathbf{R}^{-1}\mathbf{M}(\vec{p'})^{-1}\mathbf{M}(\vec{p})\mathbf{R}\boldsymbol{S}_{\mathrm{sp}} \\
&= \boldsymbol{S}_{\mathrm{sp}} + \mathbf{R}^{-1}\delta\mathbf{M}\mathbf{R}\boldsymbol{S}_{\mathrm{sp}},
\end{aligned}
\tag{A1}
$$

where $\delta\mathbf{M} = \mathbf{M}(\vec{p'})^{-1}\mathbf{M}(\vec{p}) - \mathbf{I}$, $\mathbf{I}$ is the identity matrix. The term $\mathbf{R}^{-1}\delta\mathbf{M}\mathbf{R}\boldsymbol{S}_{\mathrm{sp}}$ is then the error introduced by the polarization calibration procedure.

If $\theta_+, \theta_-, \epsilon_0, \epsilon_1 \ll 1$, the first-order perturbation of $\mathbf{M}$ is

$$
\delta\mathbf{M} \approx
\begin{pmatrix}
-2\delta G & -2\delta\gamma & -\delta\theta_- & \delta\epsilon_- \\
-2\delta\gamma & -2\delta G & 0 & \delta\epsilon_+ \\
-\delta\theta_- & 0 & -2\delta G & -2\delta\varphi \\
\delta\epsilon_- & -\delta\epsilon_+ & 2\delta\varphi & -2\delta G
\end{pmatrix}.
\tag{A2}
$$

We can then write down the expression for the error,

$$
\mathbf{R}^{-1}(\phi + \delta\phi)\delta\mathbf{M}\mathbf{R}(\phi) \approx
$$

$$
\begin{pmatrix}
-2\delta G & -(2\delta\gamma\cos 2\phi - \delta\theta_-\sin 2\phi) & -\delta\theta_-\cos 2\phi - 2\delta\gamma\sin 2\phi & \delta\epsilon_- \\
-(2\delta\gamma\cos 2\phi - \delta\theta_-\sin 2\phi) & -2\delta G & -2\delta\phi & \delta\epsilon_+\cos 2\phi + 2\delta\varphi\sin 2\phi \\
-\delta\theta_-\cos 2\phi - 2\delta\gamma\sin 2\phi & 2\delta\phi & -2\delta G & \delta\epsilon_+\sin 2\phi - 2\delta\varphi\cos 2\phi \\
\delta\epsilon_- & -(\delta\epsilon_+\cos 2\phi + 2\delta\varphi\sin 2\phi) & -\delta\epsilon_+\sin 2\phi + 2\delta\varphi\cos 2\phi & -2\delta G
\end{pmatrix}.
\tag{A3}
$$

The operator $\mathbf{R}$ can be combined with the effect of θ_+ (see section 3.1), so $\delta\theta_+$ behaves like $\delta\phi$ above.

REFERENCES

Araujo-Pradere, E. A., Fuller-Rowell, T. J., Spencer, P. S. J., Minter, C. F., 2007, Radio Science, 42, 3, DOI: 10.1029/2006RS003459.
Asad, K. M. B., et al., 2015, MNRAS, 451, 3709
Britton, M. C., 2000, ApJ, 532, 1240
Chang, T.-C., Pen, U.-L., Bandura, K., Peterson, J. B., 2010, Nature, 466, 463
Chang, T.-C., Pen, U.-L., 2008, PRL, 100, 091303
DuPlain, R., Ransom, S., Demorest, P., Brandt, P., Ford, J., Shelton, A. L., 2008, Proc. SPIE, 7019, 70191D
Finlay, C. C., et al., 2010, Geophys. J. Int., 183, 1216
Fuller-Rowell, T., Araujo-Pradere, E., Minter, C., Codrescu, M., Spencer, P., Robertson, D., Jacobson, A. R., 2006, Radio Science, 41, 6, DOI: 10.1029/2005RS003393.
Han, J. L., Demorest, P. B., van Straten, W., Lyne, A. G., 2009, ApJS, 181, 557
Heiles, C., 2001, PASP, 788, 1243
Hotan, A. W., van Straten, W., Manchester, R. N., 2004, PASA, 21, 302
Jelić V. et al., 2010, MNRAS, 409, 1647
Johnston, S., Hobbs, G., Vigeland, S., Kramer, M., Weisberg, J. M., Lyne, A. G., 2005, MNRAS, 364, 1397
Karastergiou, A., Kramer, M., Johnston, S., Lyne, A. G., Bhat, N. D. R., Gupta, Y., 2002, Astronomy and Astrophysics, 391, 247
Loeb, A., Wyithe, S., 2008, PRL, 100, 161301

Martí-Vidal, I., Krichbaum, T. P., Marscher, A., Alef, W., Bertarini, A., Bach, U., Schinzel, F. K., Rottmann, H., Anderson, J. M., Zensus, J. A., Bremer, M., Sanchez, S., Lindqvist, M., Mujunen, A., 2012, A&A, 542, A107
Masui, K. W., Switzer, E. R., Banavar, N., Bandura, K., Blake, C., Calin, L.-M., Chang, T.-C., Chen, X., Li, Y.-C., Liao, Y.-W., Natarajan, A., Pen, U.-L., Peterson, J. B., Shaw, J. R., Voytek, T. C., 2013, ApJ, 763, L20
Moore, D. F, Aguirre, J. E., Parsons, A. R., Jacobs, D. C, Pober, J. C., 2013, ApJ, 796, 154
Moore, D. F, et al., 2015, submitted to ApJ, arXiv:1502.05072
Oh, S. P., and Mack, K. J., 2003, MNRAS 346, 871
Perley, R. A., and Butler, B. J., 2013, ApJS, 206, 16
Srikanth, S., 2012, Personal Communication
Seo, H.-J., Dodelson, S., Marriner, J., Mcginnis, D., Stebbins, A., Stoughton, C., and Vallinotto, A., 2010, ApJ 721, 164
van Straten, W., 2004, ApJS, 152, 129
van Straten, W., 2006, ApJ, 642, 1004
van Straten, W., 2013, ApJS, 204, 13
Switzer, E. R., Masui, K. W., Bandura, K., Calin, L.-M., Chang, T.-C., Chen, X.-L., Li, Y.-C., Liao, Y.-W., Natarajan, A., Pen, U.-L., Peterson, J. B., Shaw, J. R., Voytek T. C., 2013, MNRAS, 434, L46

RADIO ASTRONOMICAL POLARIMETRY AND POINT-SOURCE CALIBRATION

W. van Straten
Netherlands Foundation for Research in Astronomy
straten@astron.nl
Draft version November 8, 2018

ABSTRACT

A mathematical framework is presented for use in the experimental determination of the polarimetric response of observatory instrumentation. Elementary principles of linear algebra are applied to model the full matrix description of the polarization measurement equation by least-squares estimation of non-linear, scalar parameters. The formalism is applied to calibrate the center element of the Parkes Multibeam receiver using observations of the millisecond pulsar, PSR J0437−4715, and the radio galaxy, 3C 218 (Hydra A).

Subject headings: methods: data analysis — instrumentation: polarimeters — polarization — pulsars: individual (PSR J0437-4715) — techniques: polarimetric

1. INTRODUCTION

Polarization measurements provide additional insight into the phenomena involved in both the emission and propagation of electromagnetic radiation. However, the processes of reception and detection introduce instrumental artifacts that must be corrected before meaningful interpretations of experimental data can be made. Ideally, the instrumental response is estimated by observing at least two calibrator sources of well-determined, polarized radiation (Hamaker, Bregman & Sault 1996). Under the assumption that the observatory apparatus respond linearly and remain stable between calibrator observations, the known instrumental response is then inverted and used to calibrate observations of other sources.

In the absence of a sufficient number of calibrator sources, instrumental calibration may in some cases be performed by fitting the available polarimetric data to a predictive model. This model must describe the observed sources of radiation, the response of the instrument, and any additional propagation effects that arise in the intervening media through which the signals are transmitted, such as the Earth's ionosphere. In order for the model to be constrained, at least one component of the applied measurement equation must vary as some function of one or more independent variables. For example, the constraining transformation may consist of the geometric projection of the antenna receptors onto the plane of the sky, which may vary during transit of the source for antennas without an equatorial mount.

For an altitude-azimuth mounted antenna, the receiver feed is rotated about the line of sight through the parallactic angle, a constraint that has been utilized in a number of previous studies, including Stinebring et al. (1984), Turlo et al. (1985), Xilouris (1991), McKinnon (1992), and Johnston (2002). In each of these cases, a matrix product is expanded to yield a set of scalar equations that describe the measured Stokes parameters as a function of parallactic angle; these are then solved using conventional techniques. This approach has two significant limitations. First, in order to simplify the derivation of the scalar equations and their partial derivatives, it is necessary to make small value approximations that are not generally valid.

Second, as any alteration of the reception model necessitates a laborious expansion of the matrix product, this approach is non-conducive to experimentation with a variety of parameterizations.

In addition to these shortcomings, other fundamental limitations and conceptual errors have been incorporated into previous treatments. For instance, Turlo et al. (1985) omit circular polarization from consideration, an oversimplification that restricts further application of their result to antenna with perfect, circularly polarized receptors. Stinebring et al. (1984), followed by Xilouris (1991) and McKinnon (1992), begin with the assumption that the complex gains of the two polarizations may be independently calibrated prior to determination of the cross-coupled antenna response. However, this approximation is accurate only when the differential gain and phase transformations commute with the antenna response matrix, a condition satisfied only when the feed receptors have well-determined, orthogonal polarizations. In general, the complex gains may be accurately quantified only after the effect of the antenna feed is included.

This error is essentially compounded in Johnston (2002) where, although the instrumental response parameters are jointly estimated, the measured data are first corrected using separately-determined, inaccurate estimates of differential gain and phase. In addition, the observed Stokes parameters are incorrectly normalized by the total intensity; a quantity such as the invariant interval must be used (Stinebring et al. 1984; Britton 2000). Finally, as only observations of an unknown source are used to constrain the instrumental response parameters, the solution derived by Johnston (2002) is not unique. Rather, as shown in Appendix B, there exists a degenerate set of solutions that can be resolved only with additional observations of one or more sources with known circular polarization and position angle.

In contrast to previous work, the treatment presented in this paper is based entirely on a full matrix description of the polarization measurement equation. All of the matrix products, including those of the required partial derivatives, are evaluated in software; therefore, no small value approximations are necessary and a variety of model spec-

ifications may be tested with relative ease. Furthermore, all of the model parameters are jointly constrained using observations of both unknown and partially known source polarizations. Following a brief mathematical review in Section 2, the method employed to solve the matrix equations is developed in Section 3. Two possible decompositions of the instrumental response are described in Section 4, one of which is applied in Section 5 to the calibration of the Multibeam receiver and downconversion system utilized by CPSR-II: the 128 MHz baseband recording and real-time processing system at the Parkes Observatory.

2. POLARIZED RADIATION AND PROPAGATION

Electromagnetic radiation is described by the two complex-valued components of the transverse electric field vector, $\boldsymbol{e}(t) = (e_0(t), e_1(t))$. The measurable properties of $\boldsymbol{e}(t)$ are represented by the coherency matrix, $\boldsymbol{\rho} = \langle \boldsymbol{e}(t) \otimes \boldsymbol{e}^\dagger(t) \rangle$, where the angular brackets denote time averaging and $\boldsymbol{e}^\dagger$ is the Hermitian transpose of $\boldsymbol{e}$. The coherency matrix may be written as a linear combination of Hermitian basis matrices (Britton 2000),

$$\boldsymbol{\rho} = \frac{1}{2}\sum_{k=0}^{3} S_k \boldsymbol{\sigma}_k = (S_0\,\boldsymbol{\sigma}_0 + \boldsymbol{S} \cdot \boldsymbol{\sigma})/2, \qquad (1)$$

where $\boldsymbol{\sigma}_0$ is the 2×2 identity matrix, $\boldsymbol{\sigma} = (\boldsymbol{\sigma}_1, \boldsymbol{\sigma}_2, \boldsymbol{\sigma}_3)$ are the Pauli spin matrices, S_0 is the total intensity, or Stokes I, and $\boldsymbol{S} = (S_1, S_2, S_3)$ is the Stokes polarization vector. As described in Appendix A, $\boldsymbol{S} = (Q, U, V)$ in the Cartesian reference frame applied in this paper. The Stokes parameters may also be expressed in terms of the coherency matrix (Hamaker 2000),

$$S_k = \mathrm{tr}(\boldsymbol{\sigma}_k\boldsymbol{\rho}), \qquad (2)$$

where $\mathrm{tr}(\mathbf{A})$ is the trace of the matrix, $\mathbf{A}$.

The propagation and reception of the electric field is represented by the transformations of linear time-invariant systems. Presented with the input signal, $\boldsymbol{e}(t)$, the output of a system is given by the convolution, $\boldsymbol{e}'(t) = \mathbf{j}(t) * \boldsymbol{e}(t)$, where $\mathbf{j}(t)$, is the complex-valued, 2×2 impulse response matrix. By the convolution theorem, this transformation is equivalent to $\boldsymbol{E}'(\omega) = \mathbf{J}(\omega)\boldsymbol{E}(\omega)$, where $\mathbf{J}$ is the familiar Jones matrix. When observed over a sufficiently narrow band, the variation of $\mathbf{J}$ with frequency is ignored, and polarimetric transformations are represented by Jones matrix multiplications in the time domain. Under the operation, $\boldsymbol{e}'(t) = \mathbf{J}\boldsymbol{e}(t)$, the coherency matrix is transformed as

$$\boldsymbol{\rho}' = \mathbf{J}\boldsymbol{\rho}\mathbf{J}^\dagger. \qquad (3)$$

This congruence transformation is called the polarization measurement equation (Hamaker 2000). It forms the basis through which measured quantities are related to the intrinsic polarizations of the sources and used to model the unknown instrumental response.

3. MAXIMUM LIKELIHOOD ESTIMATOR

To solve the polarization measurement equation using conventional methods of least-squares minimization, it is necessary to design a scalar figure-of-merit function and to calculate both its gradient and curvature with respect to scalar model parameters. Let $\boldsymbol{\eta}$ represent the vector of scalar parameters that describe the model, including the

instrumental response and the polarizations of the sources. Furthermore, let $\boldsymbol{x}$ represent the vector of independent variables that constrain the measurement equation, such as the observing frequency and epoch. Given $\boldsymbol{x}$, the model,

$$\boldsymbol{\rho}'_m(\boldsymbol{x}; \boldsymbol{\eta}); \ \ 1 \le m \le M, \qquad (4)$$

must predict the measured polarization of each source, where M is the number of sources. In the interest of brevity, the model may also be represented by $\boldsymbol{\rho}'_m(\boldsymbol{x})$.

Now consider N_m independent observations of the mth source, each made at a unique coordinate, $\boldsymbol{x}_{m,n}$, to yield the measured Stokes parameters and their estimated errors, $\{S'_k \pm \sigma_k\}_{m,n}$. The best-fit model parameters will minimize the objective merit function,

$$\chi^2(\boldsymbol{\eta}) = \sum_{m=1}^{M}\sum_{n=1}^{N_m}\sum_{k=0}^{3} \frac{[S'_{k,m,n} - S'_{k,m}(\boldsymbol{x}_{m,n}; \boldsymbol{\eta})]^2}{\sigma^2_{k,m,n}}, \qquad (5)$$

where $S'_{k,m}(\boldsymbol{x}_{m,n}; \boldsymbol{\eta}) = \mathrm{tr}[\boldsymbol{\sigma}_k\,\boldsymbol{\rho}'_m(\boldsymbol{x}_{m,n}; \boldsymbol{\eta})]$ are the Stokes parameters of the mth source as predicted by the model at $\boldsymbol{x}_{m,n}$. The gradient of χ^2 with respect to the scalar parameters, $\boldsymbol{\eta}$, has components,

$$\frac{\partial \chi^2}{\partial \eta_r} = -2\sum_{m=1}^{M}\sum_{n=1}^{N_m}\mathrm{tr}\left(\boldsymbol{\Delta}_{m,n}(\boldsymbol{\eta})\frac{\partial\boldsymbol{\rho}'_m(\boldsymbol{x}_{m,n}; \boldsymbol{\eta})}{\partial\eta_r}\right), \qquad (6)$$

where

$$\boldsymbol{\Delta}_{m,n}(\boldsymbol{\eta}) = \sum_{k=0}^{3}\frac{S'_{k,m,n} - S'_{k,m}(\boldsymbol{x}_{m,n}; \boldsymbol{\eta})}{\sigma^2_{k,m,n}}\,\boldsymbol{\sigma}_k. \qquad (7)$$

Taking an additional partial derivative yields

$$\frac{\partial^2\chi^2}{\partial\eta_s\partial\eta_r} = -2\sum_{m=1}^{M}\sum_{n=1}^{N_m}\mathrm{tr}\left(\frac{\partial\boldsymbol{\Delta}_{m,n}}{\partial\eta_s}\frac{\partial\boldsymbol{\rho}'_m(\boldsymbol{x}_{m,n})}{\partial\eta_r}\right), \qquad (8)$$

where, following the discussion in §15.5 of Numerical Recipes (Press et al. 1992), the term containing a second derivative in equation (8) has been eliminated. Using equations (5) through (8), the Levenberg-Marquardt method is applied to find the parameters that minimize $\chi^2(\boldsymbol{\eta})$.

4. PARAMETERIZATION OF THE MODEL

It remains to specify the scalar values, $\boldsymbol{\eta}$, that parameterize the polarization measurement equation as well as the partial derivatives of $\boldsymbol{\rho}'_m(\boldsymbol{x}; \boldsymbol{\eta})$ with respect to those parameters. As in equation (1), the coherency matrix, $\boldsymbol{\rho}_m$, of each input source polarization is completely specified by the four Stokes parameters, $S_{k,m}$. The partial derivatives with respect to these parameters are simply

$$\frac{\partial\boldsymbol{\rho}_m}{\partial S_{k,m}} = \frac{\boldsymbol{\sigma}_k}{2}. \qquad (9)$$

Now, let the model of the instrumental response be represented by the complex-valued 2×2 Jones matrix, $\mathbf{J}$. If $\mathbf{J}$ satisfies equation (3) then it belongs to the set of solutions given by $\mathbf{J}(\phi) = e^{i\phi}\mathbf{J}$, where $i = \sqrt{-1}$. That is, the coherency matrix is insensitive to the absolute phase of the signal and ϕ may be arbitrarily chosen, leaving seven degrees of freedom with which to describe the instrumental response. Two possible parameterizations are considered: the algebraic decomposition employed by Hamaker (2000) and the phenomenological description of Britton (2000).

4.1. *Algebraic Model*

Following Hamaker (2000), an arbitrary matrix, $\mathbf{J}$, is represented by its polar decomposition,

$$\mathbf{J} = J\,\mathbf{B}_{\hat{m}}(\beta)\,\mathbf{R}_{\hat{n}}(\phi) \qquad (10)$$

where $J = (\det \mathbf{J})^{1/2}$ and, as described in Appendix A,

$$\mathbf{B}_{\hat{m}}(\beta) = \cosh\beta\,\boldsymbol{\sigma}_0 + \sinh\beta\,\hat{\boldsymbol{m}}\cdot\boldsymbol{\sigma}, \text{ and} \qquad (11)$$

$$\mathbf{R}_{\hat{n}}(\phi) = \cos\phi\,\boldsymbol{\sigma}_0 + i\sin\phi\,\hat{\boldsymbol{n}}\cdot\boldsymbol{\sigma}. \qquad (12)$$

The phase of the complex value, J, is set to zero and, as any rotation about an arbitrary axis may be decomposed into a series of rotations about three perpendicular axes, the instrumental response is written as

$$\mathbf{J}_H = G\,\mathbf{B}_{\hat{m}}(\beta)\prod_{k=1}^{3}\mathbf{R}_{\hat{s}_k}(\phi_k), \qquad (13)$$

where $G = |J|$ is the absolute gain and $\hat{\boldsymbol{s}}_{\boldsymbol{k}}$ are the orthonormal basis vectors defined in Appendix A. Equation (11) may be written as $\mathbf{B}_{\hat{m}}(\beta) = b_0\,\boldsymbol{\sigma}_0 + \boldsymbol{b}\cdot\boldsymbol{\sigma}$, where $b_0 = \cosh\beta$ and $\boldsymbol{b} = \sinh\beta\,\hat{\boldsymbol{m}}$. Noting that $b_0 \geq 1$ and $b_0^2 = 1 + \boldsymbol{b}\cdot\boldsymbol{b}$, the three degrees of freedom of $\mathbf{B}_{\hat{m}}(\beta)$ are specified by $\boldsymbol{b} = (b_1, b_2, b_3)$. Therefore, the instrumental response is parameterized by G, b_{1-3}, and ϕ_{1-3}. The partial derivatives of $\mathbf{J}_H$ with respect to these seven parameters are calculated using products of

$$\frac{\partial\mathbf{B}_{\hat{m}}(\beta)}{\partial b_k} = \frac{b_k}{\sqrt{1+\boldsymbol{b}\cdot\boldsymbol{b}}}\,\boldsymbol{\sigma}_0 + \boldsymbol{\sigma}_k, \qquad (14)$$

and

$$\frac{\partial\mathbf{R}_{\hat{s}_k}(\phi_k)}{\partial\phi_k} = -\sin\phi_k\,\boldsymbol{\sigma}_0 + i\cos\phi_k\,\boldsymbol{\sigma}_k. \qquad (15)$$

4.2. *Phenomenological Model*

Beginning with Britton (2000), the response of an ideal feed with two orthogonally polarized receptors is given by $\mathbf{S}(\theta,\epsilon) = \mathbf{R}_{\hat{u}}(\epsilon)\mathbf{R}_{\hat{v}}(\theta)$. Here, the receptors have ellipticities equal to ϵ and mutually perpendicular orientations defined by θ. The basis vectors, $\hat{\boldsymbol{q}}$, $\hat{\boldsymbol{u}}$, and $\hat{\boldsymbol{v}}$, are defined in Appendix A. Using this notation, a receiver with non-orthogonal receptors is represented by

$$\mathbf{C} = \boldsymbol{\delta}_0\mathbf{S}(\theta_0,\epsilon_0) + \boldsymbol{\delta}_1\mathbf{S}(\theta_1,\epsilon_1), \qquad (16)$$

where $\boldsymbol{\delta}_a$ is the 2×2 selection matrix,

$$\boldsymbol{\delta}_a = \begin{pmatrix} \delta_{0a} & 0 \\ 0 & \delta_{1a} \end{pmatrix}, \qquad (17)$$

δ_{ab} is the Kronecker delta, and the product, $\boldsymbol{\delta}_a\mathbf{B}$, returns a matrix that contains only the ath row of $\mathbf{B}$. Equation (16) is equivalent to equation 16 of Britton (2000) and is used without making any first order approximations or further assumptions about the feed.

The differential gain and phase of the instrument are represented by $\mathbf{B}_{\hat{s}_1}(\gamma)$ and $\mathbf{R}_{\hat{s}_1}(\varphi)$ where, as in equations (A1) and (A2), γ and φ parameterize Lorentz boost and rotation transformations (Britton 2000). Including the absolute gain, G, the instrumental response is written as

$$\mathbf{J}_B = G\,\mathbf{B}_{\hat{s}_1}(\gamma)\mathbf{R}_{\hat{s}_1}(\varphi)\mathbf{C}. \qquad (18)$$

The partial derivatives of $\mathbf{J}_B$ with respect to its seven scalar parameters, G, γ, φ, θ_{0-1}, and ϵ_{0-1}, are calculated using equation (15) and

$$\frac{\partial\mathbf{B}_{\hat{s}_k}(\beta_k)}{\partial\beta_k} = \sinh\beta_k\,\boldsymbol{\sigma}_0 + \cosh\beta_k\,\boldsymbol{\sigma}_k. \qquad (19)$$

5. APPLICATION

Radio pulsar observations provide an excellent source of data with which to constrain the polarization measurement equation. The often highly polarized state of a pulsar signal can vary significantly as a function of pulse longitude. When integrated over a sufficient number of spin periods, mean polarimetric pulse profiles generally exhibit excellent stability on timescales much longer than those over which calibration observations are made. Consequently, multiple on-pulse longitudes from a single pulsar may be included as unique and stable input source polarizations, greatly increasing the number of available constraints when compared with non-pulsed sources. Furthermore, any non-pulsed background polarization is effectively eliminated by subtracting the off-pulse mean from each integrated pulse profile.

The millisecond pulsar, PSR J0437−4715, represents an ideal candidate for use in the regular calibration of the apparatus at the Parkes Observatory. As part of the high-precision pulsar timing program, it is often observed from rise to set, providing measurements with a wide range in parallactic angle. The model that describes these observations has the form,

$$\boldsymbol{\rho}'_m(\Phi) = \mathbf{J}\mathbf{R}_{\hat{v}}(\Phi)\boldsymbol{\rho}_m\mathbf{R}_{\hat{v}}^{\dagger}(\Phi)\mathbf{J}^{\dagger}, \qquad (20)$$

where $\mathbf{R}_{\hat{v}}(\Phi)$ is the rotation about the line of sight by the parallactic angle, Φ.

As demonstrated in Appendix B, additional calibrator observations are required in order to uniquely determine the solution to equation (20). The Parkes Multibeam receiver is equipped with a noise diode that ideally injects a 100% linearly polarized signal with a position angle of 45 degrees into the receiver feed horn. This reference source is switched using a signal generator and the observed square waveform is integrated modulo its period. Ideally, the on-pulse longitudes of the input reference signal contain additional flux with Stokes parameters given by $C_0[1,0,1,0]$, where C_0 is the reference flux density. Under this assumption, inclusion of reference signal observations breaks the degeneracy by constraining the boost, β_v, which mixes Stokes I and V, and the rotation, ϕ_v, which mixes Stokes Q and U. In a separate flux calibration procedure, the reference signal is observed simultaneously with the bright Fanaroff-Riley type I radio galaxy, 3C 218 (Hydra A), producing absolute flux estimates of both the system temperature and reference flux density, C_0.

5.1. *Observations*

Dual-polarization observations of PSR J0437−4715 and Hydra A were made on 19 and 20 July 2003 using the center element of the Parkes Multibeam receiver. Two 64 MHz bands, centered at 1341 and 1405 MHz, were two-bit sampled and processed by CPSR-II, the second generation of the Caltech-Parkes-Swinburne Recorder. In order to maintain optimal linear response during the digitization process, the detected power is monitored and the sampling thresholds are updated approximately every 30 seconds. In addition, the baseband data reduction software corrects quantization distortions to the voltage waveform using the dynamic level-setting technique (Jenet & Anderson 1998).

Phase-coherent dispersion removal is performed while synthesizing a 128-channel filterbank (Jenet et al. 1997); the Stokes parameters are then detected and integrated as a function of topocentric pulse phase. Data are averaged for five minute intervals, producing uncalibrated mean pulse profiles with 2048 phase bins, or an equivalent time resolution of approximately $2.8\,\mu s$.

The observed flux density varies significantly between pulsar and Hydra A observations, resulting in large changes to the digitization sampling thresholds. This difference is best modeled using the phenomenological decomposition of equation (18), applying separate absolute gain, differential gain, and differential phase terms to the two sets of observations. Also, in order to account for phase drifts on timescales of a few hours, the differential phase is modeled to vary as a cubic polynomial function of time. The three signal path transformations corresponding to the three observed sources are summarized in Table 1.

The flux of the pulsar also varies between observations, a result of both intrinsic intensity fluctuations and interstellar scintillation. Therefore, the measured Stokes parameters are normalized by the invariant interval,

$$S'_{\mathrm{inv}} = 2(\det \boldsymbol{\rho}'_{m,n})^{1/2} = (S_0'^2 - S'^2)^{1/2}, \qquad (21)$$

where the polarized intensity, $S' = |\boldsymbol{S}'|$. In order to avoid division by small or negative values, those data points with $S'_{\mathrm{inv}} < \sigma_0$ are discarded. Assuming that the measurement errors in each of the Stokes parameters are independent of each other, the estimated errors in the normalized Stokes parameters are given by

$$\hat{\sigma}_0^2 = S'^{-6}_{\mathrm{inv}} S'^2 (S'^2 \sigma_0^2 + S_0'^2 \sigma_s^2), \text{ and} \qquad (22)$$

$$\hat{\sigma}_k^2 = S'^{-4}_{\mathrm{inv}} [(S'^2_{\mathrm{inv}} + 2S_k'^2)\,\sigma_k^2 + S_k'^2 \sigma_{\mathrm{inv}}^2], \qquad (23)$$

where $1 \leq k \leq 3$,

$$S'^2 \sigma_s^2 = \sum_{k=1}^{3} S_k'^2 \sigma_k^2, \qquad (24)$$

and $S'^2_{\mathrm{inv}} \sigma_{\mathrm{inv}}^2 = S_0'^2 \sigma_0^2 + S'^2 \sigma_s^2$. Note that $\hat{\sigma}_0$ is approximately proportional to S' when $S' \ll S_0$. Consequently, the normalized total intensity is plotted on a separate scale in Figure 1, in which are displayed the normalized Stokes parameters from one of the 65 pulse longitudes used to constrain the model.

5.2. *Results*

Initial results indicated that the reference signal produced by the noise diode of the Parkes Multibeam receiver is not actually 100% linearly polarized. Rather, as shown in Figure 2, the reference signal consists of $\sim 90\%$ linear and 3% circular polarization, its position angle is not exactly 45 degrees (i.e. Stokes $Q \neq 0$), and it is severely depolarized at the edges of the band due to frequency aliasing during downconversion. Consequently, the reference signal cannot be trusted as a source with known position angle and degree of circular polarization. Also, approximately 7 MHz from both the top and bottom of the band must be discarded as irreversibly corrupted.

In order to constrain β_v, it is noted that Hydra A has less than 0.1% circular polarization (Roberts et al. 1975). Therefore, the off-pulse longitudes of the flux calibration observations serve as a source of negligible circular polarization in the remainder of this development. The unknown rotation about the line of sight, ϕ_v, is artificially

constrained by assuming that $\theta_0 = 0$; consequently, all position angles are measured with respect to the orientation of receptor 0. In modeling the reference signal, Stokes I is set to unity, producing an intermediate flux scale in units of the reference flux density; Stokes Q, U, and V are varied as free model parameters.

The reception model is solved independently for each of the 256 frequency channels in the two 64 MHz bands. In each channel are a total of 278 free model parameters, corresponding to the Stokes parameters of the 65 selected pulse longitudes, the 12 instrumental parameters listed in Table 1, and the 6 unknown Stokes parameters shared between the noise diode and Hydra A. These parameters are constrained by approximately 25220 measured values, primarily derived from the selected pulse longitudes of the 97 pulsar observations. Indicating a good fit in each frequency channel, the merit function is on average approximately equal to the number of degrees of freedom, ν, such that $\langle \chi^2 / \nu \rangle \sim 1.05$. Under the assumption that the errors in the measured Stokes parameters are normally distributed, the curvature matrix of equation (8) is inverted to yield the covariance matrix of the standard errors in each of the model parameters.

In Figure 3 are plotted the instrumental response parameters from one of the CPSR-II bands at the reference epoch. The linear dependence between differential phase and frequency indicates a signal path length mismatch between the two polarizations. The receptor ellipticities have an average value of ~ 5.7 degrees, corresponding to a rotation of the polarization vector about the U-axis by ~ 0.2 radians. Consequently, the degree of mixing between linear and circular polarizations reaches approximately 20% for uncalibrated signals with polarization vectors lying near the $Q - V$ plane. Clearly, this level of distortion cannot be treated as a second-order effect.

The mean polarimetric pulse profile of PSR J0437−4715 is plotted in Figure 4. Here, the position angle is equal to θ and the colatitude is given by $\pi/2 - 2\epsilon$. When compared with cylindrical coordinates, as plotted in Figure 3 of van Straten (2002), spherical coordinates offer a number of conceptual advantages. For instance, both the total and polarized intensities may be plotted on the same logarithmic scale, thereby enhancing the smaller features of these profiles. In addition, the chosen normalization allows the statistical significance of the measured quantities to be approximated without explicitly plotting the estimated error bars. Finally, the correlations between rapid transitions in position angle and dips in polarized intensity are more obviously apparent, for example, at pulse phases approximately equal to 0.26, 0.50, and 0.84. These regions are interpreted as transitions between two highly polarized, nearly orthogonal, superposed modes of radiation, possibly the natural modes of the pulsar magnetospheric plasma (Petrova 2001, and references therein).

6. CONCLUSIONS

A fundamentally different approach to modeling the reception and propagation of polarized radiation has been presented in this paper. Based on the formalism developed in Sections 3 and 4, a detailed calibration model has

been constructed from simple, modular components, incorporating multiple signal paths and source polarizations as constraints. Many of the limiting assumptions made in previous treatments have been eliminated in this analysis, enabling its application in a wider variety of experiments. This development is increasingly relevant in the context of design considerations for the next generation of radio telescopes and instrumentation. For instance, it has been proposed that the Square Kilometer Array (SKA) will be an interferometric array of a large number of low-cost antennas. Especially in the case of fixed dipole pairs, the polarizations of the receptors may be highly non-orthogonal; therefore, it is important to develop more sophisticated theories and techniques of polarimetric calibration.

Due to the current lack of a standard catalog of multi-frequency polarimetric pulse profiles, it is difficult to confirm the validity of any calibration technique. Future efforts should include the establishment of a set of well-calibrated sources, including a number of stable pulsars that are monitored on a regular basis at more than one observatory and at a variety of radio frequencies. Especially at lower frequencies, other propagation effects such as those arising in the ionosphere will have to be included in the reception model applied to these observations. Once established, a relatively short integration on a bright, calibrated pulsar could be used to quickly determine the instrumental response without the need for time-intensive techniques such as the one described in this paper.

In order that the results presented in Section 5.2 may be used to calibrate other observations, they are stored as binary table extensions of a PSRFITS file (Hotan, van Straten & Manchester 2004), a pulsar data format defined using the Flexible Image Transport System (Hanisch et al. 2001). Both the PSRFITS file format and its associated visualization and reduction software have been openly developed in an effort to facilitate the exchange of pulsar astronomical data between observatories and research groups.

As the current work is based on the Jones calculus, it is limited to describing only "non-depolarizing" or "pure" component transformations; it is not possible to represent the conversion of a fully polarized signal into a partially polarized one using Jones operators (Hamaker, Bregman & Sault 1996). This is demonstrated by noting that $\det(\mathbf{AB}) = \det(\mathbf{A})\det(\mathbf{B})$ and, for a fully polarized signal, $\det(\boldsymbol{\rho}) = 0$. Certain components of the instrumental apparatus may not be pure and therefore may require a Mueller matrix in order to model their effect. For example, the process of two-bit quantization may act to depolarize strong input signals, an effect that has yet to be studied in rigorous detail. Other phenomenon, such as bandwidth depolarization, may not require a Mueller matrix description if they can be treated by the application of phase-coherent matrix convolution (van Straten 2002).

The formalism developed in this paper may be equally well applied to the polarimetric calibration of a phased array. In this case, it is not necessary to describe the complete instrument in terms of the complex gains, orientations, and ellipticities of its individual receptors. Rather, it is more useful to consider only the total instrumental transformation given by the sum of the Jones matrices of the individual antennas. This development will be the subject of future work.

APPENDIX

GEOMETRIC INTERPRETATION

The 2×2 complex matrices with unit determinant may be parameterized by $\exp[(\beta\,\hat{\boldsymbol{m}} + i\phi\,\hat{\boldsymbol{n}})\!\cdot\!\boldsymbol{\sigma}]$. The unit vectors, $\hat{\boldsymbol{m}}$ and $\hat{\boldsymbol{n}}$, as well as the dimensionless values, β and ϕ, have meaningful geometric interpretations in the four-dimensional space of the Stokes parameters. Under the congruence transformation of equation (3), the Hermitian matrices,

$$\mathbf{B}_{\hat{\boldsymbol{m}}}(\beta) = \exp(\beta\,\hat{\boldsymbol{m}}\cdot\boldsymbol{\sigma}) = \cosh\beta\,\boldsymbol{\sigma}_0 + \sinh\beta\,\hat{\boldsymbol{m}}\cdot\boldsymbol{\sigma}, \tag{A1}$$

effect a Lorentz boost of the Stokes 4-vector along the axis $\hat{\boldsymbol{m}}$ by an impact parameter 2β. Likewise, the unitary matrices,

$$\mathbf{R}_{\hat{\boldsymbol{n}}}(\phi) = \exp(i\phi\,\hat{\boldsymbol{n}}\cdot\boldsymbol{\sigma}) = \cos\phi\,\boldsymbol{\sigma}_0 + i\sin\phi\,\hat{\boldsymbol{n}}\cdot\boldsymbol{\sigma}, \tag{A2}$$

rotate the Stokes polarization vector about the axis $\hat{\boldsymbol{n}}$ by an angle 2ϕ. In applying this geometric representation, the following conventions are used. First, the Pauli spin matrices are defined as

$$\boldsymbol{\sigma}_1 = \begin{pmatrix} 1 & 0 \\ 0 & -1 \end{pmatrix} \boldsymbol{\sigma}_2 = \begin{pmatrix} 0 & 1 \\ 1 & 0 \end{pmatrix} \boldsymbol{\sigma}_3 = \begin{pmatrix} 0 & -i \\ i & 0 \end{pmatrix}. \tag{A3}$$

Second, the three-dimensional space of the Stokes polarization vector, $\boldsymbol{S} = (S_1, S_2, S_3)$, is spanned by the orthonormal basis vectors, $\hat{\boldsymbol{s}}_{\boldsymbol{k}}$, such that $\hat{\boldsymbol{s}}_{\boldsymbol{k}} \cdot \boldsymbol{S} = S_k$ and $\hat{\boldsymbol{s}}_{\boldsymbol{k}} \cdot \boldsymbol{\sigma} = \boldsymbol{\sigma}_k$. Finally, Stokes Q, U, and V are calculated by the projection of $\boldsymbol{S}$ onto the Stokes unit vectors, $\hat{\boldsymbol{q}}$, $\hat{\boldsymbol{u}}$, and $\hat{\boldsymbol{v}}$, respectively. This relationship is summarized by $\boldsymbol{p} = (Q, U, V) = \mathbf{R}^T\boldsymbol{S}$, where $\mathbf{R} = (\hat{\boldsymbol{q}}\,\hat{\boldsymbol{u}}\,\hat{\boldsymbol{v}})$ is a three-dimensional rotation matrix with columns defined by the Stokes unit vectors. The orientation of these basis vectors with respect to $\hat{\boldsymbol{s}}_{\boldsymbol{k}}$ depends upon the reference frame in which the electric field vector is represented. In the Cartesian basis, the plane wave propagates along the z-axis, the electric field is decomposed into its projection along the x and y axes, and $\mathbf{R}$ is equal to the 3×3 identity matrix.

W. van Straten

Table 1

Signal Path Transformations

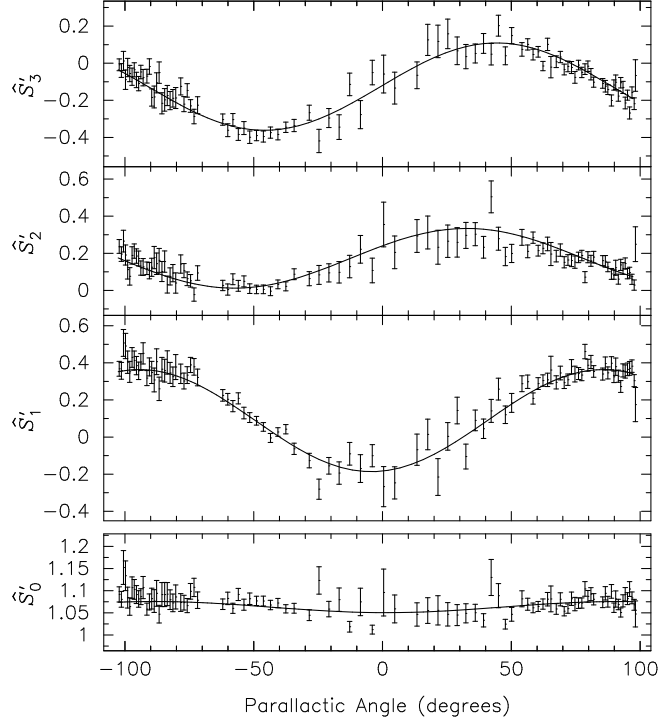| Source	Transformation
Noise Diode	$\mathbf{J}(t) = G\,\mathbf{B}_{\hat{s}_1}(\gamma)\mathbf{R}_{\hat{s}_1}(\varphi(t))\mathbf{C}$
PSR J0437−4715	$\mathbf{J}(t)\mathbf{R}_{\hat{v}}(\Phi)$
3C 218	$G_H\mathbf{B}_{\hat{s}_1}(\gamma_H)\mathbf{R}_{\hat{s}_1}(\varphi_H)\mathbf{C}$

Fig. 1.— Observed Stokes parameters from PSR J0437−4715, normalized by the invariant interval and plotted as a function of parallactic angle. These data correspond to a pulse phase of approximately 0.485 in Figure 4, as observed in a single 500 kHz channel centered at 1324.75 MHz. The Stokes parameters predicted by the best-fit model are drawn with solid lines.
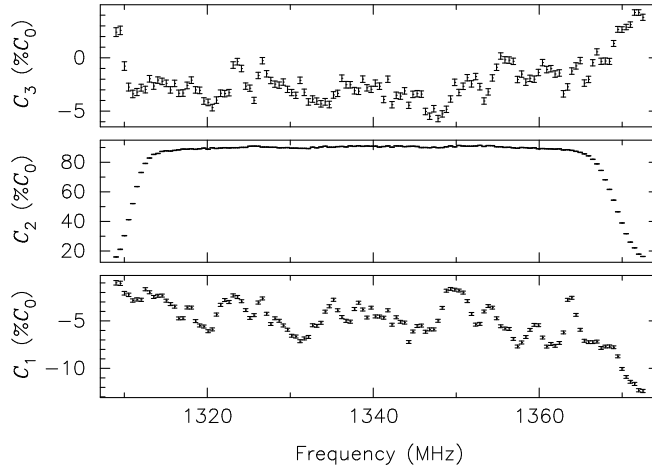

Fig. 2.— Stokes parameters of the noise diode reference signal, plotted as a function of observing frequency. The modeled values of Stokes Q, U, and V (C_1, C_2, and C_3) are specified as percentages of the reference flux density, C_0. Error bars correspond to the formal standard deviations of the model parameters derived from the best-fit covariance matrix.
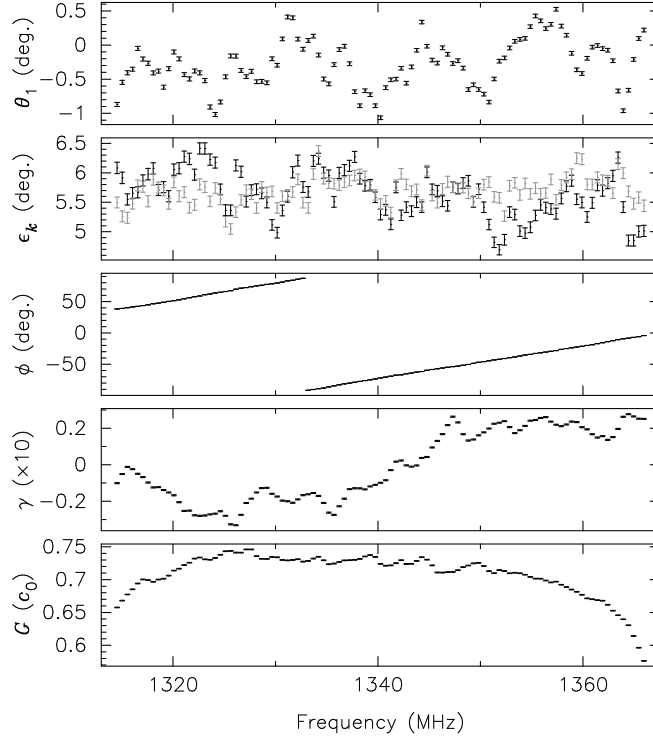
FIG. 3.— Best-fit model parameters as a function of observing frequency. From top to bottom are plotted the orientation of receptor 1 with respect to receptor 0, θ_1, the ellipticities of the receptors, ϵ_k, the differential phase, $\phi = \varphi(0)$, the differential gain, γ, and the absolute gain, G, specified in units of the square root of the reference flux density, $c_0 = \sqrt{C_0}$. In the panel showing the ellipticities, black and grey correspond to receptors 0 and 1, respectively. As in Figure 2, error bars correspond to the formal standard errors of the model parameters.
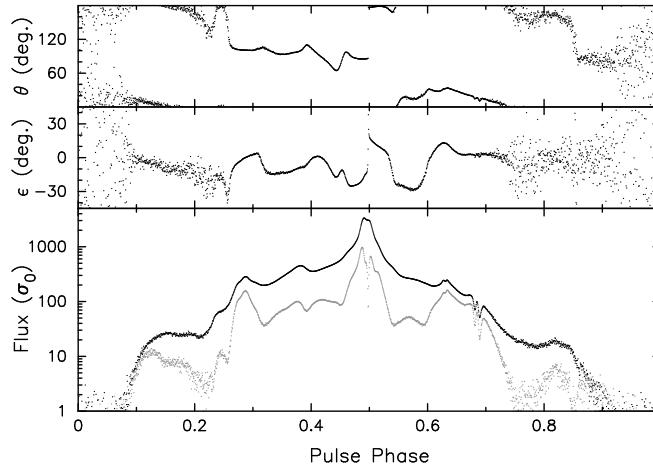

FIG. 4.— Mean polarization of PSR J0437−4715, plotted as a function of pulse phase using polar coordinates: orientation, θ, ellipticity, ϵ, and polarized intensity, $S = |\boldsymbol{S}|$ (plotted in grey below the total intensity, S_0). Flux densities are normalized by σ_0, the r.m.s. of the off-pulse total intensity phase bins. Data were integrated over a 64 MHz band centered at 1341 MHz for approximately 8 hours.

DEGENERACY UNDER COMMUTATION

The Pauli spin matrices satisfy $\boldsymbol{\sigma}_i\,\boldsymbol{\sigma}_j = \delta_{ij}\,\boldsymbol{\sigma}_0 + i\epsilon_{ijk}\,\boldsymbol{\sigma}_k$, where ϵ_{ijk} is the permutation symbol and summation over the index k is implied. Using this identity, the product of two arbitrary matrices, $\mathbf{A}$ and $\mathbf{B}$, may be expanded to yield

$$\mathbf{A}\mathbf{B} = (a\,\boldsymbol{\sigma}_0 + \boldsymbol{a}\cdot\boldsymbol{\sigma})(b\,\boldsymbol{\sigma}_0 + \boldsymbol{b}\cdot\boldsymbol{\sigma}) = (ab + \boldsymbol{a}\cdot\boldsymbol{b})\boldsymbol{\sigma}_0 + (a\boldsymbol{b} + b\boldsymbol{a} + i\,\boldsymbol{a}\times\boldsymbol{b})\cdot\boldsymbol{\sigma}. \tag{B1}$$

In this form, it can be seen that $\mathbf{A}$ and $\mathbf{B}$ commute if and only if $\boldsymbol{a}$ and $\boldsymbol{b}$ are collinear, enabling simple statements to be made regarding the uniqueness of solutions to the polarization measurement equation.

For example, consider the parallactic angle rotation given by $\mathbf{R}_{\hat{\boldsymbol{v}}}(\Phi) = \cos\Phi\,\boldsymbol{\sigma}_0 + i\sin\Phi\,\hat{\boldsymbol{v}}\cdot\boldsymbol{\sigma}$. As illustrated by equation (B1), any matrix of the form, $\mathbf{V} = V_0\,\boldsymbol{\sigma}_0 + V\hat{\boldsymbol{v}}\cdot\boldsymbol{\sigma}$, commutes freely with $\mathbf{R}_{\hat{\boldsymbol{v}}}(\Phi)$. Therefore, if both $\mathbf{J}$ and $\boldsymbol{\rho}_m$ satisfy equation (20), then $\mathbf{J}^v = \mathbf{J}\mathbf{V}^{-1}$ and $\boldsymbol{\rho}_m^v = \mathbf{V}\boldsymbol{\rho}_m\mathbf{V}^{\dagger}$ are also solutions to this equation. This degeneracy exists regardless of the parameterization of $\mathbf{J}$ or $\boldsymbol{\rho}_m$, proving that no unique solution to the polarization measurement equation may be derived solely from observations of unknown sources at multiple parallactic angles.

The consequences of this degeneracy are illustrated by noting that $\mathbf{V}$ is unimodular and may be decomposed into a boost along the $\hat{\boldsymbol{v}}$ axis, $\mathbf{B}_{\hat{\boldsymbol{v}}}(\beta_v)$, and a rotation about this axis, $\mathbf{R}_{\hat{\boldsymbol{v}}}(\phi_v)$. That is, unless $\mathbf{V}$ is determined through some other means, there remains an unknown position angle error as well as an unknown degree of mixing between the total intensity and circular polarization. An observation of a (possibly unpolarized) source with a well-determined degree of circular polarization may be used to determine β_v; additionally, an observation of a linearly polarized source with a known position angle (such as the noise diode included in many receiver packages) may be used to constrain ϕ_v.

REFERENCES

Britton M. C., 2000, ApJ, 532, 1240
Hamaker J. P., Bregman J. D., Sault R. J., 1996, A&AS, 117, 137
Hamaker J. P., 2000, A&AS, 143, 515
Hanisch R. J., Farris A., Greisen E. W., Pence W. D., Schlesinger B. M., Teuben P. J., Thompson R. W., Warnock A., 2001, A&A, 376, 359
Hotan A., van Straten W., Manchester R. N., 2004, A&A, *submitted*
Jenet F. A., Anderson S. B., 1998, PASP, 110, 1467
Jenet F. A., Cook W. R., Prince T. A., Unwin S. C., 1997, PASP, 109, 707
Johnston S., 2002, Proc. Astr. Soc. Aust., 19, 277
McKinnon M. M., 1992, A&A, 260, 533

Petrova S. A., 2001, A&A, 378, 883
Press W. H., Teukolsky S. A., Vetterling W. T., Flannery B. P., 1992, Numerical Recipes: The Art of Scientific Computing, 2nd edition. Cambridge University Press, Cambridge
Roberts J. A., Cooke D. J., Murray J. D., Cooper B. F. C., Roger R. S., Ribes J.-C., Biraud F., 1975, Aust. J. Phys., 28, 325
Stinebring D. R., Cordes J. M., Rankin J. M., Weisberg J. M., Boriakoff V., 1984, ApJS, 55, 247
Turlo Z., Forkert T., Sieber W., Wilson W., 1985, A&A, 142, 181
van Straten W., 2002, ApJ, 568, 436
Xilouris K. M., 1991, A&A, 248, 323

Single Dish Polarization Calibration

Simon Johnston

School of Physics, University of Sydney, NSW 2006, Australia

Abstract

Using the formalism of Hamaker et al. (1996), I derive a method for the polarization calibration of observations made with a single radio telescope. This method is particularly appropriate for observations of pulsars, where the sign and magnitude of the circular polarization are useful for understanding the emission processes at work. I apply the method to observations of PSR J1359–6038 made using the multibeam receiver on the Parkes radio telescope.

1 Introduction

The polarization properties of astronomical sources are interesting for a number of reasons. They can be used, for example, in determining the physical processes at work; thermal sources are not polarized, whereas non-thermal sources may have a significant degree of polarization. The rotation measure of a source can be used to determine magnetic field strengths; for example pulsar rotation measures are used to derive magnetic maps of the Galaxy. However, the degree of polarization in astronomical sources is often small, particularly circular polarization, and so careful calibration is necessary before the results can be interpreted.

Recent papers on polarization calibration of radio telescopes include those by Hamaker et al. (1996) and Britton (2000). The Hamaker et al. (1996) paper lays down the mathematical foundations which are subsequently used by Sault et al. (1996) to construct a method for instrumental calibration of a radio interferometer. Their method is routinely applied to data from the Australia Telescope Compact Array and incorporated in the software package MIRIAD. In this paper, I will use the approach of Hamaker et al. (1996) to develop a method for calibration of single dish data. This method is particularly useful for observations of pulsars. In the final section of the paper I apply the method to observations of the pulsar PSR J1359–6038 using the 20-cm multibeam receiver on the Parkes radio telescope and discuss the results.

arXiv:astro-ph/0205038v1 3 May 2002

2 Representation

Following Hamaker et al. (1996) I describe the propagation of an electromagnetic wave in the xyz coordinate system by

$$e_2 = \left< \begin{pmatrix} e_x \\ e_y \end{pmatrix} \right> \tag{1}$$

where the axis of propagation is the z axis, and e_x and e_y are complex. The coherency properties of the electric field can be expressed in xy coordinates by the coherency matrix (Born & Wolf 1964)

$$e = \left< \begin{pmatrix} e_x e_x^* \\ e_x e_y^* \\ e_y e_x^* \\ e_y e_y^* \end{pmatrix} \right> \tag{2}$$

where the $*$ denotes the complex conjugate. The electromagnetic field is converted to electric voltage in the *feed* of a radio telescope which, in the case of linear feeds, consists of two input probes aligned along x and y. A correlator multiplies and averages these voltages to produce the voltage vectors

$$v_2 = \left< \begin{pmatrix} v_x \\ v_y \end{pmatrix} \right>; \quad v = \left< \begin{pmatrix} v_x v_x^* \\ v_x v_y^* \\ v_y v_x^* \\ v_y v_y^* \end{pmatrix} \right> \tag{3}$$

Generally, one is interested in the (true) Stokes parameters, I, Q, U and V which in combination form the Stokes vector e^S. One can express e^S in terms of the electric field vector, e, by

$$e^S = \begin{pmatrix} I \\ Q \\ U \\ V \end{pmatrix} = Te; \quad T = \begin{pmatrix} 1 & 0 & 0 & 1 \\ 1 & 0 & 0 & -1 \\ 0 & 1 & 1 & 0 \\ 0 & -i & i & 0 \end{pmatrix} \tag{4}$$

The propagation of the radiation from the astrophysical source of interest to the output from the correlator can be described in the following way (Hamaker et al. 1996). Let the effects of Faraday Rotation (both through the interstellar medium and the ionosphere) and parallactic angle rotation be combined into the matrix R. We let the matrix F represent the feed response (including gains, phases and leakage terms). Hence the voltages at the two probes can be described by

$$v_2 = F \ R \tag{5}$$

and the correlator voltage vector is given by

$$v = (F \otimes F^*) \ (R \otimes R^*) \ T^{-1} \ e^S \tag{6}$$

2

where $\otimes$ denotes the Kronecker (or outer) product (Hamaker et al. 1996). The rotation matrix, R, and the feed response matrix, F, are given by Hamaker et al. (1996) as

$$R = \begin{pmatrix} \cos\phi & -\sin\phi \\ \sin\phi & \cos\phi \end{pmatrix}; \quad F = \begin{pmatrix} G & B \\ -C & H \end{pmatrix} \tag{7}$$

where each of B, C, G and H are complex terms. It is important to note that Hamaker et al. (1996) have shown that such a formalism does not involve any approximations, although often, as below, the matrices are then expanded only to first order.

In this formalism, however, unlike that of Britton (2000), there is no direct physical association of the variables B, C, G and H. B and C can be thought of as 'leakage' terms; they describe the leakage of the opposite polarization into either receptor. The real parts of G and H relate to the sensitivity of the two probes and the difference in the imaginary parts of G and H relates to the phase offset between the two channels (often called 'instrumental phase' for a pair of linear receptors). However, this is not strictly correct, as G and H also mixed with the leakage terms (Hamaker et al. 1996).

Expanding equation 6 and ignoring (for now) the effects of rotation we thus obtain

$$\begin{pmatrix} v_{xx^*} \\ v_{xy^*} \\ v_{yx^*} \\ v_{yy^*} \end{pmatrix} = \frac{1}{2} \begin{pmatrix} GG^* & GB^* & BG^* & BB^* \\ -GC^* & GH^* & -BC^* & BH^* \\ -CG^* & -CB^* & HG^* & HB^* \\ CC^* & -CH^* & -HC^* & HH^* \end{pmatrix} \begin{pmatrix} 1 & 1 & 0 & 0 \\ 0 & 0 & 1 & i \\ 0 & 0 & 1 & -i \\ 1 & -1 & 0 & 0 \end{pmatrix} \begin{pmatrix} I \\ Q \\ U \\ V \end{pmatrix} \tag{8}$$

where the scaling factor $1/2$ arises from the determinant of T. Multiplying the two 4x4 matrices together we arrive at

$$\begin{pmatrix} v_{xx^*} \\ v_{xy^*} \\ v_{yx^*} \\ v_{yy^*} \end{pmatrix} = \frac{1}{2} \begin{pmatrix} GG^* + BB^* & GG^* - BB^* & GB^* + BG^* & i(GB^* - BG^*) \\ -GC^* + BH^* & -GC^* - BH^* & GH^* - BC^* & i(GH^* + BC^*) \\ -CG^* + HB^* & -CG^* - HB^* & -CB^* + HG^* & -i(CB^* + HG^*) \\ CC^* + HH^* & CC^* - HH^* & -CH^* - HC^* & -i(CH^* - HC^*) \end{pmatrix} \begin{pmatrix} I \\ Q \\ U \\ V \end{pmatrix} \tag{9}$$

3 Measured Stokes Parameters

Using equation 9 above and defining the measured Stokes parameters in the case of linear feeds by

$$\begin{aligned} I_m &= v_{xx^*} + v_{yy^*} \tag{10} \\ Q_m &= v_{xx^*} - v_{yy^*} \\ U_m &= v_{xy^*} + v_{yx^*} \\ iV_m &= v_{xy^*} - v_{yx^*} \end{aligned}$$

we can express the measured Stokes parameters in terms of the true Stokes parameters as follows:

$$I_m = \frac{1}{2}I(g_1^2 + g_2^2 + h_1^2 + h_2^2) + \frac{1}{2}Q(g_1^2 + g_2^2 - h_1^2 - h_2^2) + \tag{11}$$

3

$$Q_m = \begin{aligned} &U(g_1 b_1 + g_2 b_2 - h_1 c_1 - h_2 c_2) + V(g_1 b_2 - g_2 b_1 + h_1 c_1 - h_2 c_2) \\ &\frac{1}{2}I(g_1^2 + g_2^2 - h_1^2 - h_2^2) + \frac{1}{2}Q(g_1^2 + g_2^2 + h_1^2 + h_2^2) + \\ &U(g_1 b_1 + g_2 b_2 + h_1 c_1 + h_2 c_2) + V(g_1 b_2 - g_2 b_1 - h_1 c_2 + h_2 c_1) \end{aligned}$$

$$U_m = \begin{aligned} &I(h_1 b_1 + h_2 b_2 - g_1 c_1 - g_2 c_2) + Q(-g_1 c_1 - g_2 c_2 - h_1 b_1 - h_2 b_2) + \\ &U(g_1 h_1 + g_2 h_2) + V(g_1 h_2 - g_2 h_1) \end{aligned}$$

$$V_m = \begin{aligned} &I(g_1 c_2 - g_2 c_1 + h_1 b_2 - h_2 b_1) + Q(g_1 c_2 + g_2 c_1 - h_1 b_2 + h_2 b_1) + \\ &U(-g_1 h_2 + g_2 h_1) + V(g_1 h_1 + g_2 h_2) \end{aligned}$$

where all second order terms in B and C have been omitted. Somewhat unconventionally I have defined each complex term above by e.g. $G = g_1 + ig_2$ rather than $G = g_1 e^{ig_2}$ to simplify the notation. Note that these parameters are assumed to be time-independent but will not, in general, be frequency independent. In a perfect system one has $b_1 = b_2 = 0$, $c_1 = c_2 = 0$, $g_1 = h_1 = 1$ and $g_2 = h_2 = 0$ and hence the measured Stokes parameters are identically equal to the true Stokes parameters (ignoring the effects of rotation of Stokes Q into U along the line of sight).

If the gains and instrumental phase have been solved for by some other method, as is often the case, (e.g. through observations of a polarized calibration signal injected directly into the feed), then $g_1 = h_1 = 1$ and $g_2 = h_2 = 0$ and equation 11 simplifies to:

$$
\begin{aligned}
I_m &= I + U(b_1 - c_1) + V(b_2 + c_2) \\
Q_m &= Q + U(b_1 + c_1) + V(b_2 - c_2) \\
U_m &= U + I(b_1 - c_1) - Q(b_1 + c_1) \\
V_m &= V + I(b_2 + c_2) - Q(b_2 - c_2)
\end{aligned}
\tag{12}
$$

We also note, as Britton (2000) has done, that a relationship holds between the measured and true Stokes parameters via

$$I_m^2 - Q_m^2 - U_m^2 - V_m^2 = K(I^2 - Q^2 - U^2 - V^2) \tag{13}$$

where K is time-invariant and is related to the determinant of the matrix in Equation 11. This expression, the so-called invariant interval, is not frequency-invariant however, as it depends on the (frequency dependent) terms in the F matrix. Britton's idea of using the invariant interval for timing purposes has been used to great effect by van Straten et al. (2001).

4   Effects of feed rotation

It is sometimes stated that performing a (short) observation, rotating the feed through $90°$ and observing again and summing the two observations has the effect of cancelling the effect of the leakage parameters. However, this is not the case, even to first order. The effect of feed rotation effectively converts Q to $-Q$ and U to $-U$. To sum the

two observations one essentially averages the sum of the two values of I_m and V_m and averages the differences of the two Q_m and U_m measurements. Assuming the gains are correctly calibrated, then using equation 12 above, one obtains:

$$
\begin{aligned}
I_m &= I + V(b_2 + c_2) \\
Q_m &= Q + U(b_1 + c_1) \\
U_m &= U - Q(b_1 + c_1) \\
V_m &= V + I(b_2 + c_2)
\end{aligned}
\tag{14}
$$

and the total linear polarization is thus

$$
L_m = L\sqrt{1 + (b_1 + c_1)^2}
\tag{15}
$$

These last two equations show that the measured Stokes parameters are now a better approximation to the true Stokes parameters than a single observation would yield. However, even though the error in I_m and L_m are likely to be small, the error in V_m can potentially be large if V is small and $b_2 + c_2$ is significant. The error in the position angle of the linear polarization will be of order $\tan^{-1}(b_1 + c_1)$.

A further potentially interesting measurement is to subtract V_m from one observation with that from an observation where the feed is rotated through $90°$. In this case one obtains

$$
V_m = -Q(b_2 - c_2)
\tag{16}
$$

If Q is large, one can then obtain $b_2 - c_2$ directly.

5   Effects of observing a polarized calibration signal

It is often the case that a cal probe is included in the receiver package. This probe usually injects a signal between the two (linear) probes at an angle of $45°$ to both. The cal thus has $I = U$ and $Q = V = 0$. Imagine now that the two probes have identical gains and there is no instrumental rotation (i.e. we can set $g_1 = h_1 = 1$ and $g_2 = h_2 = 0$). Then, if the leakage terms are present, observations of the cal will yield a signal

$$
\begin{aligned}
v_{xx^*} &= \frac{1}{2}U(1 + 2b_1) \\
v_{yy^*} &= \frac{1}{2}U(1 - 2c_1) \\
V_m &= U(b_2 + c_2)
\end{aligned}
\tag{17}
$$

The first two expressions look like gain difference between the two probes, and the presence of V looks like instrumental rotation of U into V. Hence, even though we

started with a system with perfect gains and phases, we derive using equation 12:

$$g_1 = \frac{1}{1 + 2b_1} \tag{18}$$

$$h_1 = \frac{1}{1 - 2c_1}$$

$$h_2 = b_2 + c_2$$

and hence the system looks impure! One then re-observes the cal (or any other pure U signal) with these terms in equation 11 and one obtains:

$$I_m = U\left(1 - \frac{b_1}{(1 + 2b_1)^2} + \frac{c_1}{(1 + 2c_1)^2} + \frac{1}{2}b_2^2 - \frac{1}{2}c_2^2\right) \tag{19}$$

$$Q_m = U\left(\frac{-b_1}{(1 + 2b_1)^2} + \frac{c_1}{(1 + 2c_1)^2} + \frac{1}{2}b_2^2 - \frac{1}{2}c_2^2\right)$$

$$U_m = U\left(\frac{b_1 + 2b_1^2 - c_1 + 2c_1^2 + 1}{(1 + 2b_1)(1 - 2c_1)} + b_2(b_2 + c_2)\right)$$

$$V_m = U\left(\frac{2b_2(c_1 + b_1)}{(1 + 2b_1)(1 - 2c_1)} - b_1(b_2 + c_2)\right)$$

This implies that one does not, in general, measure a pure U signal in spite of the calibration procedure.

6 Circular Feeds

The Parkes radio telescope has receivers with linear feeds. However, many other telescopes have circular feed systems. To apply this method to receivers with circular feeds one needs to change the Stokes vector e^S to

$$e^S = \begin{pmatrix} I \\ V \\ Q \\ U \end{pmatrix} \tag{20}$$

and equation 10 to read

$$I_m = v_{rr*} + v_{ll*} \tag{21}$$

$$V_m = v_{rr*} - v_{ll*}$$

$$Q_m = v_{rl*} + v_{lr*}$$

$$iU_m = v_{rl*} - v_{lr*}$$

The algebra can then be worked through to obtain expressions for the measured Stokes parameters in terms of the true parameters as in equation 11.

7 Application

From equation 11 it can be seen there are 4 measured quantities (the Stokes parameters) and a total of 12 unknowns. These 12 unknowns comprise the 4 leakage parameters (b_1, b_2, c_1, c_2), the 4 gain terms (g_1, g_2, h_1, h_2), the total intensity, linear and circular polarization of the source and an unknown angle ϕ which deals with rotation along the line of sight such that $Q = L\cos\phi$ and $U = L\sin\phi$. This angle is made up of the intrinsic position angle of the source, the rotation measure through the interstellar medium and ionosphere, the parallactic angle and the feed angle(s) with respect to some reference frame. Of these angles, only the ionospheric rotation measure and the parallactic angle are time variable. Unless some independent measurement can be made of the ionosphere, this introduces unwanted noise into the calibration matrices. Ignoring this, rotating the feed relative to the sky (for example as naturally occurs with a feed mounted on an alt-az telescope) can be used to determine the 12 unknowns. Provided we have sufficient independent measurements of the Stokes parameters at a variety of parallactic angles, we can, in principle, determine all the unknowns. Sault et al. (1996) show that observations of an unpolarized source will yield only 9 of the unknowns, but that observations of a strongly linearly polarized source can determine all 12.

Pulsars make ideal sources for (self-)calibration as they are generally highly linearly polarized and have a reasonable degree of circular polarization. Furthermore, the polarization changes across the pulse profile and one can thus use the information in multiple phase bins at a given pointing to help solve for the unknowns. The main drawback to using pulsars as calibrators is that they scintillate which implies that the total intensity, I, can vary significantly on timescales of order minutes. The fractional polarization is not affected by scintillation, however, and therefore to overcome this problem one is forced to normalise the measured Stokes parameters by I_m at the expense of being unable to measure the true value of I. Unfortunately this procedure introduces errors as, of course, I_m is not equal to I. In practice these errors will be small unless the source is highly polarized and $b_1 - c_1$ is large.

A previous method for calibration of pulsar signals was given in the Appendix of Stinebring et al. (1984) and is still in use (e.g. Weisberg et al. 1999). However, their method involves a number of simplifications and assumptions which, in my view, are incorrect in some cases and which are, in any case, no longer necessary to make. Any least squares fitting algorithm can easily solve for 12 unknowns with $\sim$100 data points in a matter of seconds and the full equations should thus be used.

Data on PSR J1359–6038 were collected on two separate occasions in July and Novmeber 2000. Each observing session lasted approximately 10 days and we obtained 65 and 66 independent observations covering the whole parallactic angle range available (approximately $\pm 94°$). These data were taken using the 64-m Parkes telescope using the centre beam of the multibeam receiver at a central observing frequency of 1318 MHz and with a total bandwidth of 128 MHz. At the start of the observing session observations were made of the flux calibrator Hydra A to obtain the system equivalent flux density. Then, a 90 sec observation of the cal signal was made followed immediately by a 3 min observation of the pulsar. The pulsar observation was calibrated

for differential gain and phase in the two probes based on the results from the cal observation and flux calibrated from the observations of Hydra A. Pulse profiles were formed in each of I_m, Q_m, U_m and V_m with 256 phase-bins per profile and 8 frequency channels across the 128 MHz total bandwidth. Q_m, U_m and V_m were then normalised by I_m.

Figure 1 shows the measured (normalised) Stokes parameters as a function of parallactic angle from data taken in November 2000 from the peak of the pulse profile in one of the frequency channels centered at 1365 MHz. It can clearly be seen that the circular polarization, V_m, varies significantly with parallactic angle and that the variations are in phase with the variations in Q_m. The deviation in V_m is very large with a peak-to-peak amplitude of about 0.2. The implication of this (from equation 12) is that $b_2 - c_2$ is of this order, given that Q_m is about unity.
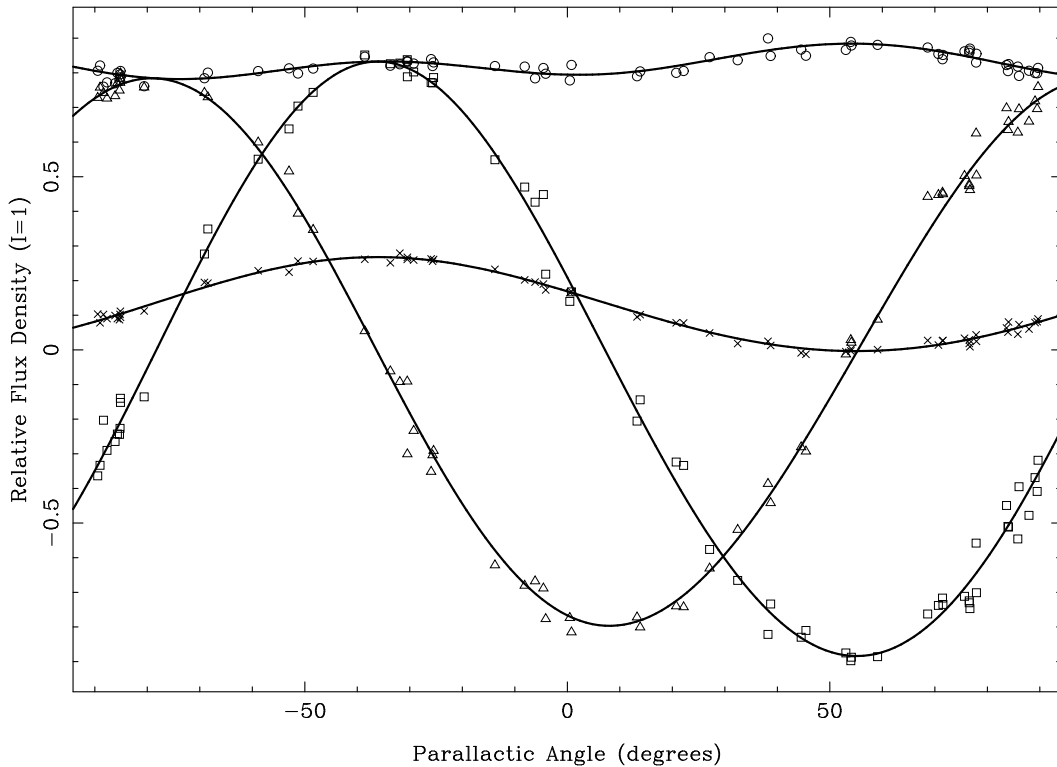

Figure 1: Measured Stokes parameters for PSR J1359–6038 as a function of parallactic angle. Here, L_m is denoted by circles, Q_m by squares, U_m by triangles and V_m by crosses. The lines denote the best fit to the data after solving equation 11.

It was shown in section 5, that observations of the cal induces subsequent errors in the observed Stokes parameters. These errors can be removed by (re-)solving for the gains and phase terms (although nominally the cal observations are used to set these) using equation 11. Practically, however, I set $g_1 = 1$ and $h_1 = 0$ and leave

8

them fixed; g_2 and h_2 then measure the relative gain and phase differences between the two probes. I then used a least squares fitting algorithm (in this case the Levenberg-Maquart Method; LMM) to minimise the residuals of $(|Q_m - Q| + |U_m - U| + |V_m - V|)$ and solve for the 9 unknowns from equation 11 given the data (remembering that I_m is fixed at 1, all the observed Stokes parameters are normalised by I_m and $g_1 = 1$, $h_1 = 0$). The result of the fitting is shown in the Figure. At this particular frequency, $b_1 = 0.0$, $b_2 = -0.05$, $c_1 = 0.02$ and $c_2 = 0.12$. Given this and the discussion in Section 4, rotating the feed through 90° and observing again still induces a leakage of I into V of order 7%, about the same size as the true V signal in many pulsars. As pointed out, an independent measurement of $b_2 - c_2$ can be obtained in this way, and confirms the measurements derived above.
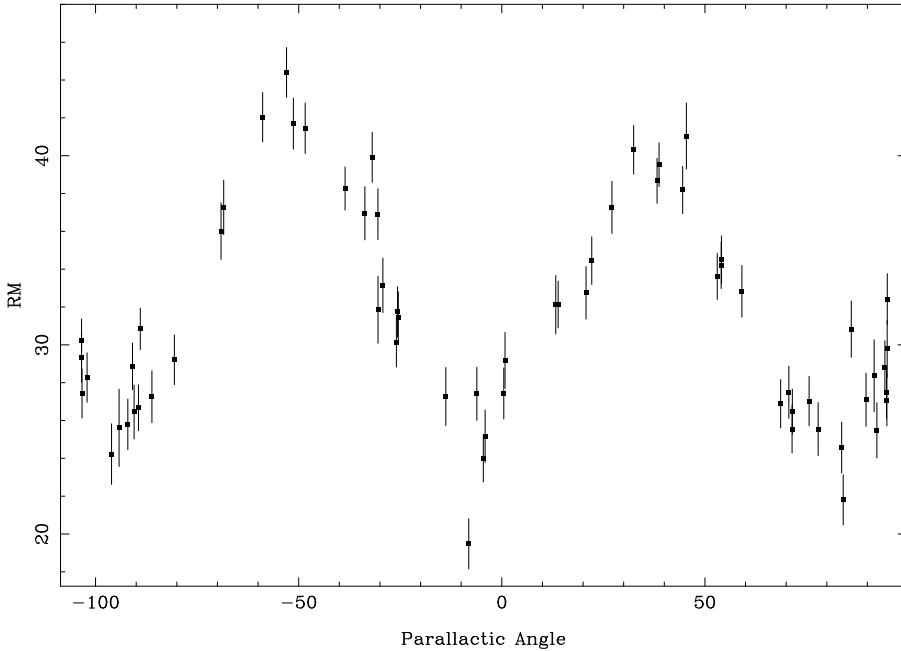

Figure 2: Rotation measure of PSR J1359–6038 as a function of parallactic angle before polarization calibration. The error bars are formal errors from the fitting process used to determine the RM.

At this point, all the parameters of the matrix form of Equation 11 have effectively been determined. The true Stokes parameters can then be obtained by multiplying the observed Stokes parameters with the inversion of this matrix. This can be achieved with e.g. the numerical recipes routine LUBKSB.

Figure 2 shows the rotation measure of the pulsar as a function of parallactic angle prior to polarization calibration. There are clear systematics in the data with sinusoidal variations of ~ 10 rad m^{-2} about a mean of 35 rad m^{-2}. These are due to the frequency dependency of the leakage terms B and C. Figure 3 shows the effects of the calibration.

9

The mean rotation measure is now 16 rad m^{-2} and the systematic effects are largely absent.
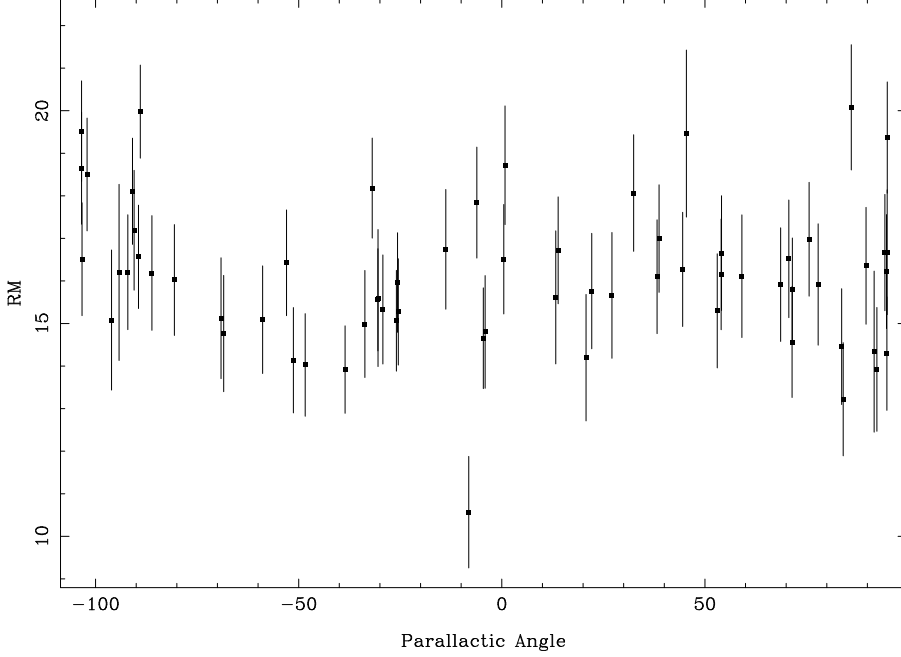

Figure 3: Rotation measure of PSR J1359–6038 after polarization calibration.

8   Conclusions

Using the excellent Hamaker et al. (1996) paper as a mathematical foundation, I have derived the matrices linking the true Stokes parameters to the observed Stokes parameters for single dish observations. It is then a computationally trivial task to solve for the terms in this matrix by least squares minimisation and thus provide a polarization calibration of the feed and receiver system.

Acknowledgments

References

Born, M. Wolf, E. 1964, Principles of Optics. Pergamon Press.

Britton, M. 2000, ApJ, 532, 1240

Hamaker, J. P., Bregman, J. D. Sault, R. J. 1996, A&ASS, 117, 137

Sault, R. J., Hamaker, J. P. Bregman, J. D. 1996, A&ASS, 117, 149

Stinebring, D. R., Cordes, J. M., Rankin, J. M., Weisberg, J. M. Boriakoff, V. 1984, ApJSS, 55, 247

van Straten, W., Bailes, M., Britton, M., Kulkarni, S. R., Anderson, S. B., Manchester, R. N., Sarkissian, J. 2001, Nature, 452, 158.

Weisberg et al., 1999, ApJSS, 121, 171

Radio Astronomical Polarimetry and the Lorentz Group

M. C. Britton

Swinburne Centre for Astrophysics and Supercomputing, Swinburne University of Technology,
Hawthorn, Victoria 3122, Australia

ABSTRACT

In radio astronomy the polarimetric properties of radiation are often modified during propagation and reception. Effects such as Faraday rotation, receiver cross-talk, and differential amplification act to change the state of polarized radiation. A general description of such transformations is useful for the investigation of these effects and for the interpretation and calibration of polarimetric observations. Such a description is provided by the Lorentz group, which is intimately related to the transformation properties of polarized radiation. In this paper the transformations that commonly arise in radio astronomy are analyzed in the context of this group. This analysis is then used to construct a model for the propagation and reception of radio waves. The implications of this model for radio astronomical polarimetry are discussed.

Subject headings: polarization — techniques: polarimetric

1. Introduction

In radio astronomy transformations occur during the propagation and reception of radio waves that act to change the state of polarized radiation. Some of these transformations, such as Faraday rotation in the ionosphere or the interstellar medium, arise from propagation effects that may themselves be of astrophysical interest. Others originate from instrumental effects such as differential amplification or receiver cross-talk, and have an adverse effect on polarimetric observations. Realistically many such effects may be present, each having its own time and frequency dependence, and collectively acting to distort measurements of the polarized radiation. The interpretation and calibration of these observations may be quite complex, and it is useful to have a general context in which to describe these transformations.

Linear transformations of fully polarized radiation were first investigated by Jones (1941), who represented transformations of the two-component transverse electric field in terms of 2x2 complex matrices now called Jones matrices. This analysis was extended to partially polarized radiation by Parrent & Roman (1960), who used Jones matrices to describe the transformation properties of the coherency matrix. Alternatively, both fully and partially polarized radiation may be described by the Stokes parameters, and their linear transformations may be represented in terms of 4x4 real matrices called Mueller matrices (Mueller 1948).

In fact these transformations are intimately related to the Lorentz group. This relationship arises from the fact that for a plane propagating wave Maxwell's equations admit two independent solutions, representing the two orthogonal senses of polarization. Thus polarized radiation constitutes a two state system, and the linear transformations of all such systems are described by the Lorentz group. This relationship has long been known in optics, and different aspects have been discussed by many authors (e.g. Barakat 1963, Whitney 1971, Cloude 1986, Pellat-Finet & Bausset 1992). Recent work has focused on representations of the Jones and Mueller matrices (Opatrny & Perina 1993, Brown & Bak 1995, Han, Kim & Noz 1997). Up to a multiplicative constant the set of Jones matrices constitute the group SL(2,C), which forms the spin 1/2 representation of the Lorentz group. The corresponding set of Mueller matrices constitutes the group SO(3,1) and forms the spin 1 representation of the Lorentz group. Finally, the relationship between Jones and Mueller matrices is represented through the 2-1 mapping between these two groups. SO(3,1).

The formulation of the transformation properties of polarized radiation in terms of Lorentz transformations affords considerable insight, including the interpretation of the Stokes parameters as a Lorentz 4-vector, the classification of transformations of this 4-vector as rotations or boosts, and the existence of a polarimetric analogue to the invariant interval. In this paper these concepts are reviewed in the context of radio astronomical polarimetry. Since both linear and circular bases are widely used in radio astronomy, a basis independent formulation is emphasized. This formalism is then used to construct a model for the propagation and reception of radio waves.

2. Representations of Polarized Radiation

Consider the representation of a transverse electromagnetic wave. Such a wave may be described through its two-component transverse electric field vector $\mathcal{E}(t)$. This vector may also represent the electric field in a waveguide, or the voltage in a pair of cables. The vector $\mathcal{E}(t)$ is commonly written in terms of the two-component complex analytic signal $\mathbf{E}(t)$ as $\mathcal{E}(t) = \mathrm{Re}\,[\mathbf{E}(t)\exp\{i\omega t\}]$. This construction is familiar from both optics (Born & Wolf 1980) and signal processing (Bracewell 1986).

For fully polarized radiation the analytic signal is independent of time. In this case the relative amplitudes and phases of the two components of $\mathbf{E}$ specify the state of elliptical polarization of the plane wave. For partially polarized radiation $\mathbf{E}(t)$ is time dependent, and measurable properties of the wave may instead be defined through time-averaging. Such an averaging procedure is conveniently treated through the coherency matrix (Wiener 1930, Wolf 1959). This is a 2x2 Hermitian matrix formed from the direct product of the analytic signal, and may be written as $\rho = \langle \mathbf{E}(t)\otimes\mathbf{E}^{\dagger}(t)\rangle$. Here the angular brackets denote time-averaging. As with any Hermitian matrix, the

coherency matrix may be written in terms of 4 real quantities $(S_o, \mathbf{S})$ as

$$\rho = (S_o \sigma_o + \mathbf{S} \cdot \sigma)/2 \tag{1}$$

where $\sigma_\mathbf{o}$ is the 2x2 identity matrix and σ is a 3-vector whose components are the Pauli spin matrices. These three 2x2 matrices are traceless and Hermitian with determinant -1. The 4 parameters $(S_o, \mathbf{S})$ are simply the mean Stokes parameters of the plane wave (Fano 1954), with S_o representing the total intensity.

Let us now introduce a particular basis. The electric field vector may be represented in the Cartesian basis $(\hat{x}, \hat{y}, \hat{z})$, in which $\mathcal{E}(t) = (\mathcal{E}_x(t), \mathcal{E}_y(t))$ is resolved into mutually orthogonal components, each orthogonal to the direction of propagation z of the plane wave. The corresponding analytic signal is $\mathbf{E}(t) = (E_x(t), E_y(t))$. For the 3-dimensional space of $\mathbf{S}$ the Cartesian basis $(\hat{q}, \hat{u}, \hat{v})$ is used, along with the customary representation of the Pauli matrices

$$\sigma_{\hat{q}} = \begin{pmatrix} 1 & 0 \\ 0 & -1 \end{pmatrix} \quad \sigma_{\hat{u}} = \begin{pmatrix} 0 & 1 \\ 1 & 0 \end{pmatrix} \quad \sigma_{\hat{v}} = \begin{pmatrix} 0 & -i \\ i & 0 \end{pmatrix} \tag{2}$$

To associate the coherency matrix with the Stokes parameters, we write ρ in this basis as

$$\rho = \langle \mathbf{E(t)} \otimes \mathbf{E}^\dagger(\mathbf{t}) \rangle = \begin{pmatrix} \langle E_x^*(t)E_x(t) \rangle & \langle E_x^*(t)E_y(t) \rangle \\ \langle E_y^*(t)E_x(t) \rangle & \langle E_y^*(t)E_y(t) \rangle \end{pmatrix} \tag{3}$$

From equation 1, the Stokes parameters in this basis become

$$\begin{aligned} S_o &= \langle E_x^*(t)E_x(t) \rangle + \langle E_y^*(t)E_y(t) \rangle \quad & S_u &= 2\,\mathrm{Re}\,[\langle E_x^*(t)E_y(t) \rangle] \\ S_q &= \langle E_x^*(t)E_x(t) \rangle - \langle E_y^*(t)E_y(t) \rangle \quad & S_v &= 2\,\mathrm{Im}\,[\langle E_x^*(t)E_y(t) \rangle] \end{aligned} \tag{4}$$

This is simply the usual definition of the Stokes parameters in a linear basis (Born & Wolf 1980).

3. Transformation Properties of Polarized Radiation

Let us now consider the transformation properties of polarized radiation. Attention is restricted to linear, invertible transformations. This excludes the class of projective transformations, which are important in representing perfect polarizing filters. Similarly, such transformations cannot describe multipath propagation of coherent radiation, such as the focusing or defocusing of radiation by lenses or mirrors. Despite this restriction, the set of linear, invertible transformations encompasses a broad class of physical processes, including single-particle scattering, propagation through anisotropic media, and many transformations arising from instrumental devices. This set may also describe the linear transformations of the voltage signal in two cables, which are known in linear network theory as two-port networks (Ruston & Bordogna 1966). This equivalence is particularly useful in radio astronomy, where the two

components of the electric field are converted to voltages by a receiver and then passed through an electronics downconversion chain.

The most general linear transformation of the analytic signal may be written as $\mathbf{E}'(t) = \mathbf{t}\mathbf{E}(t)$, where the Jones matrix $\mathbf{t}$ is a 2x2 complex matrix. As the direct product of the analytic signal, the coherency matrix must transform as $\rho' = \mathbf{t}\rho\,\mathbf{t}^{\dagger}$. For invertible transformations a Jones matrix may be written as $\mathbf{t} = \sqrt{\det \mathbf{t}}\,\mathbf{t}_N$, where $\det \mathbf{t}$ is the determinant of $\mathbf{t}$ and $\mathbf{t}_N$ is a matrix with unit determinant. The set of 2x2 complex invertible matrices with unit determinant forms the group SL(2,C), which constitutes the spin $1/2$ representation of the Lorentz group.

To investigate the transformation properties of the Stokes parameters, note that the determinant of equation 1 is simply $\det \rho = S_o^2 - |S|^2 \equiv S_{\mathrm{inv}}$ (Barakat 1963). This is just the form of the Lorentz invariant. Under transformation by the Jones matrix $\mathbf{t}$, $\det \rho' = |\sqrt{\det \mathbf{t}}|^2 S_{\mathrm{inv}}$, so that this interval is preserved up to a multiplicative constant. The set of transformations that preserve this interval forms the group SO(3,1), which constitutes the spin 1 representation of the Lorentz group. That is, the Stokes parameters transform as a Lorentz 4-vector, with the total intensity acting as the timelike component and the remaining Stokes parameters acting as the spacelike components. The condition that the total intensity $S_o > 0$ restricts this 4-vector to lie within or on the surface of the forward light cone. These two cases correspond to partially polarized ($S_{\mathrm{inv}} > 0$) or fully polarized ($S_{\mathrm{inv}} = 0$) radiation, respectively.

The representations of the groups SL(2,C) and SO(3,1) are well known in physics, but are not widely used in astronomy. Basis-independent representations of these groups are now reviewed, and are interpreted in the context of polarimetry. This will serve both as an introduction and to establish the notation used in the next section. For similar reviews, see Brown & Bak (1995) or Tung (1996).

The group SL(2,C) contains as a subgroup the set of 2x2 unitary transformations SU(2). Any such unitary transformation may be parameterized as

$$\mathbf{r}_{\hat{\mathbf{n}}}(\phi) = e^{(i\,\sigma\cdot\hat{\mathbf{n}}\,\phi)} = \sigma_0 \cos\phi + i\,\sigma\cdot\hat{\mathbf{n}}\,\sin\phi \tag{5}$$

where $\hat{\mathbf{n}}$ is a unit 3-vector. This is called the axis-angle parameterization of SU(2). The angle ϕ differs from the definition customary in classical and quantum mechanics by a factor of $1/2$, but is in agreement with the conventions of optics. Under the transformation of equation 5, $\rho \to \mathbf{r}_{\hat{\mathbf{n}}}(\phi)\rho\,\mathbf{r}_{\hat{\mathbf{n}}}(-\phi) = (\sigma_o S_o + \sigma\cdot\mathbf{S}')/2$, where

$$\mathbf{S}' = \mathbf{S}\cos 2\phi + \mathbf{S}\times\hat{\mathbf{n}}\sin 2\phi + (\hat{\mathbf{n}}\cdot\mathbf{S})\hat{\mathbf{n}}\,(1 - \cos 2\phi) \tag{6}$$

and we have used the relationship $(\sigma\cdot\mathbf{a})(\sigma\cdot\mathbf{b}) = \mathbf{a}\cdot\mathbf{b} + i\sigma\cdot(\mathbf{a}\times\mathbf{b})$. But $\mathbf{S}'$ is simply the vector resulting from a rotation of $\mathbf{S}$ about an axis $\hat{\mathbf{n}}$ by an angle 2ϕ (*cf.* Goldstein 1980). This reflects the well-known mapping between SU(2) and the group SO(3), whose elements form a representation of the rotations of a 3-dimensional vector. The mapping is 2-1, since the two rotations $\mathbf{r}_{\hat{\mathbf{n}}}(\phi)$ and $\mathbf{r}_{\hat{\mathbf{n}}}(\phi + \pi) = -\mathbf{r}_{\pm\hat{\mathbf{n}}}(\phi)$ result in the

same vector $\mathbf{S}'$. Such rotations preserve the degree of polarization $|\mathbf{S}|/S_o$ of the plane wave, and are readily interpreted geometrically in the space of the Poincare sphere in terms of the axis $\hat{\mathbf{n}}$ and angle 2ϕ of rotation. Equation 5 may be represented in the basis of equation 2 as

$$\mathbf{r}_{\hat{\mathbf{n}}}(\phi) = \begin{pmatrix} \cos\phi + in_q \sin\phi & (in_u + n_v)\sin\phi \\ (in_u - n_v)\sin\phi & \cos\phi - in_q \sin\phi \end{pmatrix} \tag{7}$$

where $\hat{\mathbf{n}} = (n_{\hat{q}}, n_{\hat{u}}, n_{\hat{v}})$. From equation 6 the corresponding rotation of the Stokes parameters (S_o, S_q, S_u, S_v) in this basis is

$$\mathbf{R}_{\hat{\mathbf{n}}}(2\phi) = \begin{pmatrix} 1 & 0 & 0 & 0 \\ 0 & n_q^2 + (1 - n_q^2)\cos 2\phi & n_q n_u \sin^2\phi + n_v \sin 2\phi & n_q n_v \sin^2\phi - n_u \sin 2\phi \\ 0 & n_q n_u \sin^2\phi - n_v \sin 2\phi & n_u^2 + (1 - n_u^2)\cos 2\phi & n_u n_v \sin^2\phi + n_q \sin 2\phi \\ 0 & n_q n_v \sin^2\phi + n_u \sin 2\phi & n_u n_v \sin^2\phi - n_q \sin 2\phi & n_v^2 + (1 - n_v^2)\cos 2\phi \end{pmatrix} \tag{8}$$

For example, for $(n_{\hat{q}}, n_{\hat{u}}, n_{\hat{v}}) = (1, 0, 0)$ equation 8 constitutes the rotation about the $\hat{q}$ axis $\mathbf{R}_{\hat{\mathbf{q}}}(2\phi)$, which may be interpreted from equation 7 as generating a phase delay between the two components of the electric field.

Next let us consider the group SL(2,C), which has a parameterization similar to its subgroup SU(2). Any element of the group may be written as $\exp(i\sigma \cdot \hat{\mathbf{n}}\,\phi + \sigma \cdot \hat{\mathbf{m}}\,\beta)$, where $\hat{\mathbf{n}}$ and $\hat{\mathbf{m}}$ are unit vectors. In analogy with equation 5, let us consider transformations for which $\phi = 0$. Such transformations may be written in terms of the Hermitian matrix

$$\mathbf{b}_{\hat{\mathbf{m}}}(\beta) = \exp(\sigma \cdot \hat{\mathbf{m}}\,\beta) = \sigma_0 \cosh\beta + \sigma \cdot \hat{\mathbf{m}} \sinh\beta \tag{9}$$

Under this transformation the coherency matrix becomes $\rho \to \mathbf{b}_{\hat{\mathbf{m}}}(\beta)\rho\,\mathbf{b}_{\hat{\mathbf{m}}}(\beta) = (\sigma_o S_o' + \sigma \cdot \mathbf{S}')/2$, where

$$S_o' = S_o \cosh 2\beta + \mathbf{S} \cdot \hat{\mathbf{m}} \sinh 2\beta$$
$$\mathbf{S}' = \mathbf{S} + \left(S_o \sinh 2\beta + 2\mathbf{S} \cdot \hat{\mathbf{m}} \sinh^2\beta\right)\hat{\mathbf{m}} \tag{10}$$

This is simply the result of performing a Lorentz boost on the 4-vector $S = (S_o, \mathbf{S})$ along the axis $\hat{\mathbf{m}}$ by a velocity parameter 2β (cf. Jackson 1975). As in the general case, such a transformation preserves the invariant interval S_{inv}. Unlike rotations, it does not preserve the degree of polarization $|\mathbf{S}|/S_o$ of the plane wave. For example, there exists some transformation that will completely depolarize partially polarized radiation. This is just the analogue of the statement in special relativity that there always exists a reference frame in which two events separated by a timelike interval occur at the same position in space. Equation 9 may be represented in the basis of equation 2 as

$$\mathbf{b}_{\hat{\mathbf{m}}}(\beta) = \begin{pmatrix} \cosh\beta + m_q \sinh\beta & (m_u - im_v)\sinh\beta \\ (m_u + im_v)\sinh\beta & \cosh\beta - m_q \sinh\beta \end{pmatrix} \tag{11}$$

where $\hat{\mathbf{m}} = (m_{\hat{q}}, m_{\hat{u}}, m_{\hat{v}})$. The boost of equation 10 in this basis becomes

$$\mathbf{B}_{\hat{\mathbf{m}}}(2\beta) = \begin{pmatrix} \cosh 2\beta & m_q \sinh 2\beta & m_u \sinh 2\beta & m_v \sinh 2\beta \\ m_q \sinh 2\beta & 1 + 2m_q^2 \sinh^2 \beta & 2m_q m_u \sinh^2 \beta & 2m_q m_v \sinh^2 \beta \\ m_u \sinh 2\beta & 2m_q m_u \sinh^2 \beta & 1 + 2m_u^2 \sinh^2 \beta & 2m_u m_v \sinh^2 \beta \\ m_v \sinh 2\beta & 2m_q m_v \sinh^2 \beta & 2m_u m_v \sinh^2 \beta & 1 + 2m_v^2 \sinh^2 \beta \end{pmatrix} \quad (12)$$

The rotations of equations 7 and 8 and boosts of equation 11 and 12 constitute a subset of the Lorentz transformations that suffices for the radio astronomical applications presented in the next section.

Finally, systems consisting of multiple physical processes are readily modelled through successive application of the above transformations. Of particular use in the analysis of such composite systems are the commutation relations

$$[\mathbf{R}_{\hat{\mathbf{n}}}(\alpha)\mathbf{R}_{\hat{\mathbf{n}}}(\beta)] = [\mathbf{R}_{\hat{\mathbf{n}}}(\alpha)\mathbf{B}_{\hat{\mathbf{n}}}(\beta)] = [\mathbf{B}_{\hat{\mathbf{n}}}(\alpha)\mathbf{B}_{\hat{\mathbf{n}}}(\beta)] = 0 \quad (13)$$

As we shall see in the next section, these relationships are useful in determining whether the transformations that arise from different physical processes or instrumental elements commute with one another.

4. The Propagation and Reception of Radio Waves

Let us examine some practical situations in which linear, invertible transformations of polarized radiation arise. One such example is a rotation of the electric field vector about the direction of propagation. This transformation may represent a rotation of a physical device with respect to the plane wave. Another example arises from Faraday rotation, which occurs when radio waves propagate through a magnetized plasma. Such a transformation may be written as $\mathbf{r}_{\hat{v}}(\phi)$. Equivalently, the transformation of the Stokes parameters is $\mathbf{R}_{\hat{v}}(2\phi)$. A similar transformation generates a phase delay between the two components of $\mathbf{E}$, and may be written as the rotation $\mathbf{r}_{\hat{q}}(\psi)$. In optics a physical device that induces such a phase delay is called a compensator. This transformation arises in electronics when two signals traverse different cable lengths. Both $\mathbf{r}_{\hat{v}}(\phi)$ and $\mathbf{r}_{\hat{q}}(\psi)$ are unitary, and preserve the degree of polarization $|\mathbf{S}|/S_o$ and the invariant interval S_{inv}.

Differential amplification or attenuation of the components of $\mathbf{E}$ provide examples of a non-unitary transformation. Consider the transformation

$$\mathbf{g} = \begin{pmatrix} g_a & 0 \\ 0 & g_b \end{pmatrix} \quad (14)$$

We may write this as $\mathbf{g} = \sqrt{g_a g_b}\, \mathbf{b}_{\hat{q}}(\beta)$, where $\beta = \ln(g_b/g_a)$. The Stokes parameters transform as $g_a g_b \mathbf{B}_{\hat{q}}(2\beta)$. Note that this transformation does not preserve $|\mathbf{S}|/S_o$, and preserves S_{inv} only up to the factor $g_a g_b$.

Next consider two orthogonal elliptically polarized waves with axial ratio $\tan\chi$ and orientation θ (Chandrasekhar 1960).

$$e_a = \left(\begin{array}{c} \cos\theta\cos\chi - i\sin\theta\sin\chi \\ -\sin\theta\cos\chi - i\cos\theta\sin\chi \end{array} \right) \quad e_b = \left(\begin{array}{c} \sin\theta\cos\chi - i\cos\theta\sin\chi \\ \cos\theta\cos\chi + i\sin\theta\sin\chi \end{array} \right) \quad (15)$$

We may perform a change of basis by forming a matrix $\mathbf{s}$ with rows $e_a^\dagger$ and $e_b^\dagger$. This matrix may be factored as $\mathbf{s}(\theta,\chi) = \mathbf{r}_{\hat{u}}(\chi)\mathbf{r}_{\hat{v}}(\theta)$. A transformation from a linear to a circular basis occurs for $\chi = \pi/4$, and in the case where $\theta = \pi/4$ results simply in a cyclic permutation of the indices $(\hat{q},\hat{u},\hat{v}) \to (\hat{v},\hat{q},\hat{u})$ in equation 2. The transformation $\mathbf{s}(\theta,\chi)$ may also be regarded as representing a receiver with two receptors sensitive to orthogonal forms of elliptical radiation. The process of reception constitutes a projection of $\mathbf{E}$ onto the receptors of the receiver, which is represented by matrix multiplication of $\mathbf{E}$ by $\mathbf{s}(\theta,\chi)$. Clearly the choice of a rotation about the $\hat{u}$ axis followed by one about the $\hat{v}$ axis is not unique. One alternative specification of elliptically polarized radiation is given in terms of an orientation and phase delay as $\mathbf{r}_{\hat{v}}(\theta)\mathbf{r}_{\hat{q}}(\phi)$. In optics this transformation is accomplished through a device known as a Babinet compensator (Born & Wolf 1980).

Now let us consider a receiver sensitive to two forms of elliptical polarization that are not necessarily orthogonal. This situation may arise in practice from imperfections in the construction of a receiver (Conway & Kronberg 1969, Stinebring et al. 1984). The transformation may be written as

$$\mathbf{c} = \left(\begin{array}{cc} \cos\theta_a\cos\chi_a + i\sin\theta_a\sin\chi_a & -\sin\theta_a\cos\chi_a + i\cos\theta_a\sin\chi_a \\ \sin\theta_b\cos\chi_b + i\cos\theta_b\sin\chi_b & \cos\theta_b\cos\chi_b - i\sin\theta_b\sin\chi_b \end{array} \right) \quad (16)$$

where the two probes of the receiver are sensitive to elliptical radiation with axial ratios χ_a, χ_b and orientations θ_a, θ_b. For the case $\theta_a = \theta_b$ and $\chi_a = \chi_b$ equation 16 simplifies to the unitary transformation $\mathbf{s}(\theta,\chi)$. In the general case such a transformation does not conserve energy. With the definitions

$$\begin{array}{cc} \sigma_\theta = \theta_a + \theta_b & \sigma_\chi = \chi_a + \chi_b \\ \delta_\theta = \theta_a - \theta_b & \delta_\chi = \chi_a - \chi_b \end{array} \quad (17)$$

we may write $\mathbf{c} = \mathbf{c}'\mathbf{r}_{\hat{v}}(\sigma_\theta/2)$, where

$$\mathbf{c}' = \left(\begin{array}{cc} \cos(\sigma_\chi/2 + \delta_\chi/2)\cos\delta_\theta/2+ & -\cos(\sigma_\chi/2 + \delta_\chi/2)\sin\delta_\theta/2+ \\ i\sin(\sigma_\chi/2 + \delta_\chi/2)\sin\delta_\theta/2 & i\sin(\sigma_\chi/2 + \delta_\chi/2)\cos\delta_\theta/2 \\ -\cos(\sigma_\chi/2 - \delta_\chi/2)\sin\delta_\theta/2+ & \cos(\sigma_\chi/2 - \delta_\chi/2)\cos\delta_\theta/2+ \\ i\sin(\sigma_\chi/2 - \delta_\chi/2)\cos\delta_\theta/2 & i\sin(\sigma_\chi/2 - \delta_\chi/2)\sin\delta_\theta/2 \end{array} \right) \quad (18)$$

For a nearly orthogonal receiver with receptors sensitive to linearly polarized radiation, this matrix may be written to first order in these parameters as

$\mathbf{c}' = \mathbf{b}_{\hat{u}}^{(1)}(\delta_\theta/2)\mathbf{b}_{\hat{v}}^{(1)}(\delta_\chi/2)\mathbf{r}_{\hat{u}}^{(1)}(\sigma_\chi/2)$. Here the superscript (1) indicates that these transformations are first order in their arguments.

These examples may be combined to form a model for the propagation and reception of radio waves.

$$\mathbf{t} = \sqrt{g_a g_b}\,\mathbf{b}_{\hat{q}}(\beta)\mathbf{r}_{\hat{q}}(\Phi_I)\mathbf{b}_{\hat{u}}^{(1)}(\delta_\theta/2)\mathbf{b}_{\hat{v}}^{(1)}(\delta_\chi/2)\mathbf{r}_{\hat{u}}^{(1)}(\sigma_\chi/2)\mathbf{r}_{\hat{v}}(\sigma_\theta/2)\mathbf{r}_{\hat{v}}(\zeta)\mathbf{r}_{\hat{v}}(\Phi_{\mathrm{iono}})\mathbf{r}_{\hat{v}}(\Phi_{\mathrm{ISM}})$$
$$\tag{19}$$

where Φ_{iono} and Φ_{ISM} are the angles arising from Faraday rotation in the ionosphere and the interstellar medium, respectively, ζ is the angle between the frame of the receiver and that of the sky, and Φ_I is the instrumental phase delay arising from differing electronic pathlengths. The equivalent transformation law for the Stokes parameters is simply obtained from equation 19.

$$S' = g_a g_b \mathbf{B}_{\hat{q}}(2\beta)\mathbf{R}_{\hat{q}}(2\Phi_I)\mathbf{B}_{\hat{u}}^{(1)}(\delta_\theta)\mathbf{B}_{\hat{v}}^{(1)}(\delta_\chi)\mathbf{R}_{\hat{u}}^{(1)}(\sigma_\chi)\mathbf{R}_{\hat{v}}(\sigma_\theta)\mathbf{R}_{\hat{v}}(2\zeta)\mathbf{R}_{\hat{v}}(2\Phi_{\mathrm{iono}})\mathbf{R}_{\hat{v}}(2\Phi_{\mathrm{ISM}})\,S$$
$$\tag{20}$$

The analysis of this model is simplified through the commutation relations in equation 13. Amplifications and phase delays in the downconversion chain represent boosts and rotations with respect to the $\hat{q}$ axis, so it is easy to see that the order of amplifiers and relative electronics delays does not matter. Terms from individual components may simply be collected into the overall parameters β and Φ_I. Similarly, rotations about the same axis commute, and rotations about the $\hat{v}$ axis by the angles ζ, Φ_{iono}, and Φ_{ISM} all have the same signature. Note that each of the parameters in this model may have its own time and frequency dependence. For example, Φ_{iono} fluctuates in time as the ionospheric column density changes, and scales as ν^{-2} from the cold plasma dispersion relation. Finally, calibration of a polarimetric observation is accomplished through the inversion of equations 19 or 20. Naturally such an inversion requires a knowledge of the parameters in this model.

5. Discussion

The representation of polarimetric transformations in terms of the Lorentz group provide a simple context in which to analyze polarized radiation. This formalism is particularly relevant for the calibration of polarimetric data, and greatly simplifies the discussion from a qualitative standpoint. Propagation or instrumental effects that give rise to the rotations of equation 8 change the polarized component of the radiation $\mathbf{S}$, thus obscuring the properties of the true, emitted light. Those effects that take the form of a boost transformation mix the total intensity S_o and the polarized component of the radiation $\mathbf{S}$. Such transformations can have a particularly detrimental effect on polarimetric observations. In many astrophysical applications S_o is much larger than $|\mathbf{S}|$, so that even boosts nearly equivalent to the identity matrix may completely corrupt the polarized flux. Observations that aim to detect very small polarized fractions,

such as the polarized component of the Cosmic Microwave Background radiation or the circularly polarized radio emission from Active Galactic Nuclei, are particularly vulnerable. For applications that require extremely high precision, the mixing of $\mathbf{S}$ into S_o can corrupt an observation. One such example has been seen in high-precision pulsar timing, where differential amplification and receiver cross-talk induce time dependent mixing of the pulse profiles, thereby modifying the total intensity profile and systematically shifting the times of arrival (Britton et al., in preparation). For pulsar observations the invariant S_{inv} proves particularly useful, since an invariant pulse profile may be formed that is independent of propagation and instrumental effects. This invariant profile may then be used for timing or to investigate pulse variability that may be intrinsic to the pulsar.

REFERENCES

Barakat, R. 1963, J. Opt. Soc. Am. 53, 317

Born, M. & Wolf, E. 1980, "Principles of Optics" (Cambridge: University Press)

Bracewell, R. N. 1986, "The Fourier Transform and its Applications" (New York: McGraw Hill)

Brown, C. S. & Bak, A. E. 1995, Optical Engineering 34, 1625

Chandrasekhar, S. 1960, "Radiative Transfer" (New York: Dover)

Cloude, S. R. 1986, Optik, 75, 26

Conway, R. G., & Kronberg, P. P. 1969, MNRAS 142, 11

Fano, U. 1954, Phys. Rev. 93, 121

Goldstien, H. 1980, "Classical Mechanics" (Reading, Massachusetts: Addison-Wesley)

Han, D., Kim, Y. S. & Noz, M. E. 1997a, Phys. Rev. E, 56, 6065

Jackson, J.D. 1975, "Classical Electrodynamics" (New York: John Wiley & Sons)

Jones, R. C. 1941, J. Opt. Soc. Am. 31, 488

Mueller, H. 1948, J. Opt. Soc. Am. 38, 661

Opatrny, T. & Perina, J 1993, Physics Letters A, 181, 199

Parrent, G. B. & Roman, P. 1960, Nuovo Cimento, 15, 370

Pellat-Finet, P. & Bausset, M. 1992, Optik, 90, 101

Ruston, H. & Bordogna, J. 1966, "Electric Networks: functions, filters, analysis" (New York: McGraw-Hill)

Stinebring, D. R., Cordes, J. M., Rankin, J. M., Weisberg, J. M., & Boriakoff, V. 1984, ApJS, 55, 247

Whitney, C. 1971, J. Opt. Soc. Am., 61, 1207

Wiener, N. 1930, Acta Math. 55, 118

Wolf, E. 1959, Nuovo Cimento, 13, 1165

Tung, W. K. 1985, "Group Theory in Physics" (Philadelphia: World Scientific)